Banner appropriate to article type will appear here in typeset article

Wave scattering by plate array metacylinders of arbitrary cross section

Hui Liang[1]*, Richard Porter[2]* and Siming Zheng[3]†

[1]Technology Centre for Offshore and Marine, Singapore (TCOMS), 118411, Republic of Singapore

[2]School of Mathematics, Woodland Road, University of Bristol, Bristol BS8 1UG, UK

[3]Ocean College, Zhejiang University, Zhoushan, Zhejiang 316021, PR China

(Received xx; revised xx; accepted xx)

Metastructures composed of closely-spaced plate array have been widely used in bespoke manipulation of waves in contexts of acoustics, eletromagnetics, elasticity and water waves. This paper is focused on scattering of waves by discrete plate array metasctructures of arbitrary cross section, including isolated vertical metacylinders, periodic arrays, and horizontal surface-piercing metacylinders. A suitable transform-based method has been applied to each problem to reduce the influence of barriers in a two-dimensional problem to a set of points in a one-dimensional wave equation wherein the solution is constructed using a corresponding Green's function. A key difference from the existing work is the use of an exact description of the plate array rather than an effective medium approximation, enabling the exploration of wave frequencies above resonance where homogenisation models fail but where the most intriguing physical findings are unravelled. The new findings are particularly notable for graded plate array metasctructures that produce a dense spectrum of resonant frequencies, leading to broadband "rainbow reflection" effects. This study provides new ideas for the design of structures for the bespoke control of waves with the potential for innovative solutions to coastal protection schemes or wave energy converters.

Key words: Wave-structure interactions; plate-arrays; rainbow reflection; graded metamaterials

1. Introduction

Structures comprised of closely-spaced parallel arrays of thin plates are useful devices in the bespoke manipulation of waves in several physical settings including acoustics (Zhu *et al.* 2013; Jan & Porter 2018; Porter 2021; Bravo & Maury 2023), electromagnetics (Putley *et al.* 2022, 2023), elasticity (Colombi *et al.* 2016; Colquitt *et al.* 2017; Ponti *et al.* 2022) and water waves (Kucher *et al.* 2023; Zheng *et al.* 2020; Porter *et al.* 2022; Wilks *et al.* 2022; Zheng *et al.* 2024). The key underpinning feature in all such applications is how flux is restricted by the narrow channels between adjacent plates in the device, compared to the isotropic nature

† Email address for correspondence: siming.zheng@zju.edu.cn; * H.L. and R.P. contributed equally.

Abstract must not spill onto p.2

of propagation in the surrounding medium. The wavelength is thus implicitly assumed to be much larger than the characteristic separation between adjacent plates. This contrast in lengthscales and the unusual wave phenomena, such as negative refraction (Porter 2021), that can result from the anisotropy has led to such plate-array devices being classified as a type of metamaterial (Maier 2017). Additionally, the finite length of the channels within compact devices means that they typically support local resonant modes thereby allowing small devices (less than a wavelength, say, in size) to have a disproportionately large effect on the external wavefield (Zheng *et al.* 2020).

Owing to the contrast in scales, several studies have investigated the effect of plate-array metastructures on waves by replacing the discrete structure of the plate array with an effective medium after implementing a low-frequency homogenisation approach. This allows wave interaction with plate-array devices having certain simple geometrical shapes to be analysed using established mathematical techniques for solving partial differential equations. For example, rectangular and cylindrical structures lend themselves to separation methods (e.g. as considered in Porter (2021), Zheng *et al.* (2020)) and, in rare cases, mathematical methods can be applied to more complex geometries (e.g. Jan & Porter (2018) who considered a trapezoidal plate-array cavity in a waveguide wall). One of the restrictions of homogenisation, however, is that it does not apply close to internal channel resonance where local effects destroy the assumption of a contrast in scales. Thus, it has been shown in Putley *et al.* (2022) and Jan & Porter (2018) for example that the problems become ill-posed in frequency intervals where resonance is present on account of the assumptions of low-frequency homogenisation having been violated. Problems can be regularised by the introduction of a small amount of dissipation (as in Jan & Porter (2018); Zheng *et al.* (2020)) into the effective field equations, but this "sticking-plaster approach" overlooks the precise nature of the influence of the local channel scale.

In this paper we present a methodology which allows us to investigate wave interaction with structures comprised of *discrete* plate-arrays; that is without the homogenisation. Such an approach is not new: see Porter (2021) who used Fourier transform methods to compare wave scattering by an infinitely-long rectangular strip filled with a periodic array of tilted plates with the equivalent homogenisation theory. Resonant amplification is not encountered in this problem and the discrete plate array description was shown to converge rapidly to the homogenised description with near-identical results for the far-field scattered amplitudes when the channel width to length ratio fell below 0.1. Experimental results of Kucher *et al.* (2023) also supported this conclusion. The idea of using Fourier transforms also underpins the current work where the focus is on methods for determining wave scattering by more general, non-regular, metastructures. In particular, we focus on the effect on wave propagation of so-called graded plate-arrays in which the width of the channels in the device is non-constant (typically increasing linearly, and thus forming a wedge).

Graded metamaterials have been of interest to researchers in a range of different applications since they produce broadbanded effects. For example, in Colombi *et al.* (2016); Colquitt *et al.* (2017) a graded array placed on the surface of an elastic half-space was shown to deflect surface Rayleigh waves into elastic body waves and it was later proposed (e.g. Brûlé *et al.* (2020)) as a scheme for protecting infrastructure from earthquakes. In acoustics Zhu *et al.* (2013) have graded structures to provide broadbanded absorption of sound by a metasurface and Jan & Porter (2018); Bravo & Maury (2023) showed that a metamaterial plate-array cavity could suppress acoustic transmission in waveguides over a wide range of frequencies. In water waves Wilks *et al.* (2022) have similarly shown the broadbanded reflective qualities of a graded array of plates submerged through the surface and also been proposed its extension as a wave energy harnessing device. So-called rainbow reflection and rainbow trapping and absorption by graded metamaterials have also featured in the work of Tsakmakidis *et al.* (2007); Jimenez *et al.* (2017); Bennetts *et al.* (2018); Chaplain *et al.* (2020); Ponti *et al.* (2022). Circular metacylinders comprised of a plate array are also graded, although not linearly, and have exhibited (e.g. Zheng *et al.* (2020); Putley *et al.* (2023)) similar features: a slowing wave speed and amplification of wave energy through the structure with a strong broadbanded reflective quality.

We consider three problems all set in the context of linearised water waves although the first two problems have analogues in other physical settings. In all three problems oblique plane waves are scattered by metastructures consisting of a discrete plate array with elements which are arbitrary in separation and width allowing us to consider metastructures of general shape. In the first problem, described in Section 2, we consider a single such device consisting of vertical plates extending fully through the water depth. In Section 3 the second problem involves an infinite periodic array of these devices. In the final problem (Section 4) the plates extend only partially through the fluid depth, this problem being identical to that studied by Wilks *et al.* (2022).

We propose a common method of solution based on transforms (infinite Fourier for the first problem, and finite transforms for the last two) in which the solution in the presence of $N + 1$ plates of varying position and length is shown to be expressed by the same simple characteristic formulation. This simplicity, an overlooked highlight of the related work of Noad & Porter (2015), is in contrast with, for example, Wilks *et al.* (2022); Roy *et al.* (2019) who use separation solutions in each of the channel-based domains and then performed matching from one channel to the next using relatively convoluted methods.

Although there is a focus on the method of solution to these problems the main emphasis is on the results which are presented in Section 5. Here we compare discrete plate array results with existing results including those determined by homogenisation and present extensions to results inaccessible to homogenisation methods with a focus on resonance. This includes looking at the effects of graded arrays with a view to application as sea defence systems. We conclude the work in Section 6.

2. A plate array metastructure in an open domain

We consider waves on a fluid of constant depth h with a free surface whose rest position is given by $z = 0$, z being the vertical coordinate, directed upwards out of the fluid. We suppose that a parallel array of $N + 1$ thin vertical barriers occupy the surfaces $x = x_j$, $-h < z < 0$, $|y| < b_j$, for $j = 0, \ldots, N$, as illustrated in figure 1. A surface wave of angular frequency ω is incident from infinity, heading at an anti-clockwise angle θ_0 with respect to the positive x-direction. On the assumptions of linearised water wave theory, its motion and the subsequent response of the fluid due to the interaction with the array of barriers may be described by a velocity potential (e.g. Linton & McIver (2001))

$$\Phi(x, y, z, t) = \mathrm{Re}\{\phi(x, y)\psi_0(z)\mathrm{e}^{-\mathrm{i}\omega t}\} \tag{2.1}$$

where the uniformity of the geometry through the depth allows us to factorise a depth dependence

$$\psi_0(z) = N_0^{-1/2} \cosh k(z + h), \qquad \text{and} \qquad N_0 = \frac{1}{2}\left(1 + \frac{\sinh 2kh}{2kh}\right) \tag{2.2}$$

is a normalising factor whilst k is the positive real root of

$$\omega^2/g \equiv K = k \tanh kh, \tag{2.3}$$

the usual dispersion relation for water waves with gravitational acceleration given by g. The wave elevation is proportional to $\phi(x, y)$. Consequently, the reduced two-dimensional

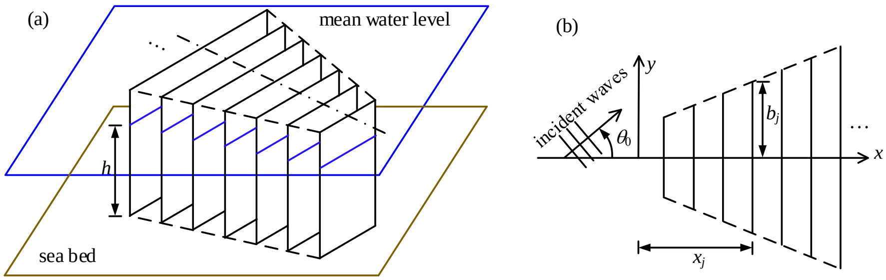

Figure 1: Sketch of wave interactions with a plate-array metastructure.

complex velocity potential $\phi(x, y)$ satisfies the wave equation

$$\left(\frac{\partial^2}{\partial x^2} + \frac{\partial^2}{\partial y^2} + k^2\right)\phi = 0. \tag{2.4}$$

Within this framework the incident wave is described by the function

$$\phi_{inc}(x, y) = \mathrm{e}^{\mathrm{i}\alpha_0 x}\mathrm{e}^{\mathrm{i}\beta_0 y} \tag{2.5}$$

where $\alpha_0 = k\cos\theta_0$, $\beta_0 = k\sin\theta_0$ and we require that $\phi(x, y) - \phi_{inc}(x, y)$ represents outgoing waves as $kr \longrightarrow \infty$ where $r = (x^2 + y^2)^{1/2}$. Specifically, we write

$$\phi(x, y) - \phi_{inc}(x, y) \sim A(\theta; \theta_0)\sqrt{\frac{2}{\pi kr}}\mathrm{e}^{\mathrm{i}kr - \mathrm{i}\pi/4} \tag{2.6}$$

where $(x, y) = r(\cos\theta, \sin\theta)$ and $A(\theta; \theta_0)$ is defined as the diffraction coefficient, measuring the amplitude of circular waves scattered in the direction θ due to an incident wave heading θ_0.

Scattering of waves is due to the presence of barriers on which the following conditions apply

$$\frac{\partial\phi}{\partial x} = 0, \qquad x = x_j^{\pm}, \qquad |y| < b_j, \quad (j = 0, \ldots, N). \tag{2.7}$$

We remark that the boundary-value problem posed above can be interpreted in physical settings other than water waves including, for example, two-dimensional acoustics or Tranverse Electrically-polarised electromagnetics, in which the factorisation of the z-dependence and the dispersion relation will both differ.

The method of solution for this problem is described in the work of Noad & Porter (2015) but we include below a key simplification to the solution method which will be reused in later sections. Thus, we introduce the Fourier transform pair

$$\bar{\phi}(x; \beta) = \int_{-\infty}^{\infty} [\phi(x, y) - \phi_{inc}(x, y)]\mathrm{e}^{-\mathrm{i}\beta y}\,\mathrm{d}y \tag{2.8}$$

and

$$\phi(x, y) = \phi_{inc}(x, y) + \frac{1}{2\pi}\int_{-\infty}^{\infty} \bar{\phi}(x; \beta)\mathrm{e}^{\mathrm{i}\beta y}\,\mathrm{d}\beta. \tag{2.9}$$

Then the governing wave equation is transformed to

$$\left(\frac{\mathrm{d}^2}{\mathrm{d}x^2} - \gamma^2\right)\bar{\phi} = 0, \qquad x \neq x_j \tag{2.10}$$

($j = 0, \ldots, N$) where

$$\gamma = \begin{cases} \sqrt{\beta^2 - k^2}, & |\beta| \geqslant k, \\ -\mathrm{i}\alpha, & |\beta| < k \end{cases} \tag{2.11}$$

where $\alpha = \sqrt{k^2 - \beta^2}$ and the choice of complex branch of the square root function is made to satisfy the radiation condition at infinity (this becomes clear only later on). We note the transformation of the barrier conditions lead to the jump conditions

$$\bar{\phi}_x(x_j^+; \beta) - \bar{\phi}_x(x_j^-; \beta) = 0 \tag{2.12}$$

and

$$\bar{\phi}(x_j^+; \beta) - \bar{\phi}(x_j^-; \beta) = P_j(\beta) \tag{2.13}$$

for $j = 0, \ldots, N$ where

$$P_j(\beta) = \int_{-b_j}^{b_j} p_j(y) \mathrm{e}^{-\mathrm{i}\beta y} \, \mathrm{d}y \tag{2.14}$$

using the definition

$$\phi(x_j^+, y) - \phi(x_j^-, y) = \begin{cases} p_j(y), & |y| < b_j, \\ 0, & |y| > b_j. \end{cases} \tag{2.15}$$

Rather than expand the solution in each of the $N + 2$ domains $x < x_0$, $x_{j-1} < x < x_j$ ($j = 1, \ldots, N$) and $x > x_N$ and match using (2.12) and (2.13), as in Noad & Porter (2015), we adopt a much more elegant approach which results in the same final expression and is easy to adapt to other problems.

Let us define the canonical function $g(x, x_j; \beta)$ as the solution of

$$\left(\frac{\mathrm{d}^2}{\mathrm{d}x^2} - \gamma^2 \right) g = 0, \qquad x \gtrless x_j \tag{2.16}$$

satisfying jump conditions $g_x(x_j^+, x_j; \beta) - g_x(x_j^-, x_j; \beta) = 0$ and $g(x_j^+, x_j; \beta) - g(x_j^-, x_j; \beta) = 1$ such that g is outgoing (when $|\beta| < k$) or exponentially decaying (when $|\beta| > k$) as $k|x - x_j| \to \infty$. It is straightforward to confirm that

$$g(x, x_j; \beta) = -\frac{1}{2} \mathrm{sgn}(x - x_j) \mathrm{e}^{-\gamma |x - x_j|}. \tag{2.17}$$

The solution of (2.10), (2.12), (2.13), with outgoing waves at infinity is given by the weighted superposition

$$\bar{\phi}(x; \beta) = \sum_{j=0}^{N} P_j(\beta) g(x, x_j; \beta) = -\frac{1}{2} \sum_{j=0}^{N} P_j(\beta) \mathrm{sgn}(x - x_j) \mathrm{e}^{-\gamma |x - x_j|}. \tag{2.18}$$

The general solution throughout the domain is given by inverting the transform, thus

$$\phi(x, y) = \phi_{inc}(x, y) - \frac{1}{4\pi} \sum_{j=0}^{N} \mathrm{sgn}(x - x_j) \int_{-\infty}^{\infty} \mathrm{e}^{-\gamma |x - x_j|} \mathrm{e}^{\mathrm{i}\beta y} \int_{-b_j}^{b_j} p_j(y') \mathrm{e}^{-\mathrm{i}\beta y'} \, \mathrm{d}y' \, \mathrm{d}\beta. \tag{2.19}$$

We note that this representation of the general solution may also be obtained by distributing Green's functions over the barriers and applying the conditions on the barriers. The particular form expressed above requires that the integral representation of the Hankel function (representing the Green's function) given by (A 2) is used and the ordering of integrals is interchanged. The advantage of using the representation (2.19) of the solution, rather than a Green's function representation, is that we encounter no technical issues relating to convergence. In contrast, the Green's function approach leads to integrals with hypersingular kernels having to be treated as Hadamard finite-part integrals (see Martin (1991) for example).

The particular solution is determined by applying the barrier conditions (2.7) which result in the coupled integral equations

$$\frac{1}{4\pi}\sum_{j=0}^{N}\int_{-\infty}^{\infty}\gamma \mathrm{e}^{-\gamma|x_j-x_k|}\mathrm{e}^{\mathrm{i}\beta y}\int_{-b_j}^{b_j}p_j(y')\mathrm{e}^{-\mathrm{i}\beta y'}\,\mathrm{d}y'\,\mathrm{d}\beta = -\mathrm{i}\alpha_0\mathrm{e}^{\mathrm{i}\alpha_0 x_k}\mathrm{e}^{\mathrm{i}\beta_0 y}, \qquad |y|<b_k \tag{2.20}$$

for $k = 0,\ldots,N$ for the $N+1$ unknown functions $p_j(y)$. We approximate solutions to (2.20) by writing

$$p_j(y) \approx \sum_{p=0}^{2Q+1} a_p^{(j)} w_p(y/b_j) \tag{2.21}$$

where Q is a truncation parameter, $a_p^{(j)}$ are designated unknown expansion coefficients, and

$$w_p(u) = \frac{\mathrm{e}^{\mathrm{i}\pi p/2}}{(p+1)\pi}\sqrt{1-u^2}\,\mathrm{U}_p(u) \tag{2.22}$$

are expansion functions where $\mathrm{U}_p(\cdot)$ represents the Chebychev polynomial of the second-kind. We note the relation (see (Gradshtyen & Ryhzik 1965, 10§3.715 (13), (18)))

$$D_p(\lambda) = \int_{-1}^{1} w_p(u)\mathrm{e}^{-\mathrm{i}\lambda u}\,\mathrm{d}u = \begin{cases}\mathrm{J}_{p+1}(\lambda)/\lambda, & \lambda\neq 0,\\ \frac{1}{2}\delta_{p0}, & \lambda = 0\end{cases} \tag{2.23}$$

and $\mathrm{J}_p(\cdot)$ is a Bessel function of order p whilst δ represents the Kronecker delta. The representation (2.21) thus accounts explicitly for the anticipated square-root behaviour in $p_j(y)$ as $|y|\to b_j^-$. We implement Galerkin's method which involves substituting (2.21) into (2.20) before multiplying by the conjugate function $w_q^*(y/b_k)$ and integrating over $|y|<b_k$, where the asterisk $*$ denotes the complex conjugate. This results in the following system of equations for the expansion coefficients:

$$\sum_{p=0}^{2Q+1}\sum_{j=0}^{N} a_p^{(j)} K_{pq}^{(jk)} = -\mathrm{i}\alpha_0 b_k \mathrm{e}^{\mathrm{i}\alpha_0 x_k} D_q(\beta_0 b_k), \qquad q = 0,\ldots,2Q{+}1,\;\; k = 0,\ldots,N \tag{2.24}$$

where

$$K_{pq}^{(jk)} = \frac{b_j b_k}{4\pi}\int_{-\infty}^{\infty}\gamma \mathrm{e}^{-\gamma|x_j-x_k|}D_p(\beta b_j)D_q(\beta b_k)\,\mathrm{d}\beta. \tag{2.25}$$

Computational savings are available by making further manipulations which, in part, reflect the symmetry about $y=0$ of the geometry and, in part, exploit the logarithmic singularity that is embedded in the formulation despite us having avoided the use of Green's functions. We note that $D_p(\lambda) = (-1)^p D_p(-\lambda)$ whilst γ is symmetric in β with $\gamma\sim|\beta|$ as $\beta\to\pm\infty$. Furthermore we note an orthogonality relation for Bessel functions (Gradshtyen & Ryhzik 1965, 10§6.5382(2))

$$\int_0^\infty \frac{\mathrm{J}_{2p+1+\nu}(u)\mathrm{J}_{2q+1+\nu}(u)}{u}\,\mathrm{d}u = \frac{1}{4p+2\nu+2}\delta_{pq} \tag{2.26}$$

for $\nu = 0, 1$. Taken together, this allows the original system (2.24) to be decoupled into the pair of second-kind systems of equations

$$\frac{1}{2\pi}\frac{a^{(k)}_{2q+\nu}}{4q+2\nu+2}+\sum_{p=0}^{Q}\sum_{j=0}^{N}a^{(j)}_{2p+\nu}\widehat{K}^{(jk)}_{2p+\nu,2q+\nu}=-\mathrm{i}\alpha_0 b_k \mathrm{e}^{\mathrm{i}\alpha_0 x_k}D_{2q+\nu}(\beta_0 b_k), \qquad \begin{cases} q=0,\ldots,Q,\\ k=0,\ldots,N\end{cases} \tag{2.27}$$

($\nu = 0, 1$ encode symmetric and antisymmetric components) where, for $k \neq j$,

$$\widehat{K}^{(jk)}_{2p+\nu,2q+\nu}=\frac{b_j b_k}{2\pi}\int_0^\infty \gamma \mathrm{e}^{-\gamma|x_j-x_k|}D_{2p+\nu}(\beta b_j)D_{2q+\nu}(\beta b_k)\,\mathrm{d}\beta \tag{2.28}$$

are dimensionless exponentially-convergent integrals whilst, for $j = k$,

$$\widehat{K}^{(jj)}_{2p+\nu,2q+\nu}=\frac{b_j^2}{2\pi}\int_0^\infty (\gamma-\beta)D_{2p+\nu}(\beta b_j)D_{2q+\nu}(\beta b_j)\,\mathrm{d}\beta \tag{2.29}$$

contain oscillatory integrands whose amplitude decays as $O(1/\beta^3)$ accelerated from a $O(1/\beta)$ decay in the original system (2.24) with (2.25). Furthermore,

$$\widehat{K}^{(jk)}_{2p+\nu,2q+\nu}=\widehat{K}^{(kj)}_{2p+\nu,2q+\nu}=\widehat{K}^{(jk)}_{2q+\nu,2p+\nu} \tag{2.30}$$

are symmetric with respect to (j, k) and (p, q) pairs.

We note that in the special arrangement $x_j = jc$ and $b_j = b$, representative of a rectangular metastructure with regular spacing between array elements,

$$\widehat{K}^{(jk)}_{2p+\nu,2q+\nu}=\frac{b^2}{2\pi}\int_0^\infty \gamma \mathrm{e}^{-\gamma|j-k|c}D_{2p+\nu}(\beta b)D_{2q+\nu}(\beta b)\,\mathrm{d}\beta \tag{2.31}$$

depends only on $|j-k| = 0, \ldots, N$ and requires only $N + 1$ integrals for each (p, q) pair, rather than $(N+1)(N+2)/2$ evaluations. Computation of the elements of the matrix system is thus an $O(N)$ task rather than $O(N^2)$ for this special case. The matrix size scales with N and although the inversion of a Toeplitz matrix can be reduced from $O(N^3)$ to $O(N^2)$ and this part of the computation remains the limiting factor as N becomes very large.

The values of $a^{(j)}_p$ are numerically determined from the solution of (2.27) where, typically, a value of $Q = 5$ is sufficient for convergence to five or more decimal places unless the frequency is high when Q must be increased. Subsequently, this allows ϕ to be determined everywhere by using

$$\phi(x,y)=\phi_{inc}(x,y)+\sum_{k=0}^{N}\sum_{p=0}^{Q}a^{(k)}_p\Lambda^{(k)}_p \tag{2.32}$$

where $\Lambda^{(k)}_p$ can be alternatively expressed as

$$\Lambda^{(k)}_p=-\frac{b_k}{4\pi}\int_{-\infty}^{\infty}\mathrm{sgn}(x-x_k)\,D_p(\beta b_k)\mathrm{e}^{-\gamma|x-x_k|+\mathrm{i}\beta y}\mathrm{d}\beta \tag{2.33}$$

or

$$\Lambda^{(k)}_p=-\frac{\mathrm{i}}{4}\int_{-b_k}^{b_k}\frac{k(x-x')}{\varrho}H_1(k\varrho)w_p(y'/b_k)\mathrm{d}y' \tag{2.34}$$

where the expression (2.34) has applied the integral representation of Hankel function, see appendix A for details. In the computation of wave field, equation (2.33) is used when $|x - x_k| > \epsilon$ due to the exponential decay factor, and expression (2.34) is adopted otherwise.

We have particular interest in the diffraction coefficient which may be calculated from (2.20) using $x = r\cos\theta$, $y = r\sin\theta$ and employing a stationary phase approximation following the parametrisation of $\beta \in (-\infty, \infty)$ as $\beta = k\sin\psi$ for $(-\pi/2, \pi/2)$ and $\beta = \pm k\cosh u$ for $u \in (0, \theta)$ via the relationship $\psi = \pm\pi/2 \mp \mathrm{i}u$. In the limit $kr \to \infty$ the dominant contribution to the far field comes from the integral over $-\pi/2 < \psi < \pi/2$ at $\psi = \theta$ or $\psi = \theta + \pi$ depending on the value of θ. Within this branch, $\gamma = -\mathrm{i}\alpha = -\mathrm{i}\cos\psi$ and it is the negative sign of the branch, chosen earlier, that dictates that the scattered waves are outgoing. After some algebra we find

$$A(\theta;\theta_0) \approx -\frac{k\cos\theta}{4}\sum_{k=0}^{N} \mathrm{e}^{-\mathrm{i}kx_k\cos\theta}\sum_{p=0}^{Q} a_p^{(k)} b_k D_p(kb_k\sin\theta) \tag{2.35}$$

and the dependence on θ_0 is embedded in the coefficients $a_p^{(k)}$ whose values are determined by the incident wave forcing in (2.27). We note that the diffraction coefficient satisfies the so-called optical theorem (Maruo 1960)

$$\sigma = \frac{1}{2\pi}\int_0^{2\pi} |A(\theta;\theta_0)|^2 \,\mathrm{d}\theta = -\mathrm{Re}[A(\theta_0;\theta_0)] \tag{2.36}$$

and represents the total scattering cross-section, or scattering energy.

We are also interested in the total hydrodynamic force in the x-direction of the j-th plate in the array which is proportional to

$$F_x^{(j)} = -\mathrm{i}\omega\rho\int_{-h}^{0}\psi_0(z)\int_{-b_j}^{b_j} p_j(y)\,\mathrm{d}y\,\mathrm{d}z \approx -\mathrm{i}\omega\rho\frac{N_0^{-1/2}\sinh kh}{2k}a_0^{(j)}b_j. \tag{2.37}$$

3. An infinite periodic array of plate array metastructures

We assume now that the metastructure considered in the previous section is repeated periodically in the y-direction with spacing between a reference point within adjacent identical structures given by $2d$. This is commonly referred to as the scattering of oblique waves by a periodic diffraction grating as described in the context of plate-array metastructures by Putley *et al.* (2022). When $\theta_0 = 0$ the periodicity allows the problem to be interpreted as geometrically equivalent to the reflection and transmission of incident waves by a single metastructure on the centreline of a uniform channel of width $2d$ with impermeable walls. However, we retain the generality of oblique incidence here and demonstrate that both the solution method and numerical procedure are very similar to that encountered in the open domain problem considered in the previous section. The usual arguments for plane wave scattering by a periodic grating follow. Thus, since $\phi_{inc}(x, y + 2d) = \mathrm{e}^{2\mathrm{i}\beta_0 d}\phi_{inc}(x, y)$ with $\beta_0 = k\sin\theta_0$ as before it also must follow that $\phi(x, y + 2d) = \mathrm{e}^{2\mathrm{i}\beta_0 d}\phi(x, y)$ and this allows one to consider the scattering problem in a fundamental cell, say $y \in [-d, d]$, $-\infty < x < \infty$ provided we also impose periodic boundary conditions on the lateral edges of the cell, these being

$$\phi(x, d) = \mathrm{e}^{2\mathrm{i}\beta_0 d}\phi(x, -d), \qquad \text{and} \qquad \phi_y(x, d) = \mathrm{e}^{2\mathrm{i}\beta_0 d}\phi_y(x, -d). \tag{3.1}$$

The extension to $y \notin [-d, d]$ is provided by $\phi(x, y + 2md) = \mathrm{e}^{2\mathrm{i}\beta_0 md}\phi(x, y)$ for $m \in \mathbb{Z}$. As well as restricting the domain to a strip of width $2d$, the far-field conditions also change to

$$\phi(x, y) - \phi_{inc}(x, y) \sim \sum_{n=-n_-}^{n_+} R_n \mathrm{e}^{-\mathrm{i}\alpha_n x}\mathrm{e}^{\mathrm{i}\beta_n y}, \qquad kx \to -\infty \tag{3.2}$$

and

$$\phi(x,y) \sim \sum_{n=-n_-}^{n_+} T_n e^{i\alpha_n x} e^{i\beta_n y}, \qquad kx \to \infty \tag{3.3}$$

where R_n, T_n are complex-valued reflection and transmission coefficients,

$$\beta_n = \beta_0 + n\pi/d, \qquad n \in \mathbb{Z} \tag{3.4}$$

and

$$\alpha_n = \sqrt{k^2 - \beta_n^2}, \qquad -n_- \leqslant n \leqslant n_+ \tag{3.5}$$

are real wavenumber components with $\alpha_0 = k\cos\theta_0$ as before and

$$n_- = \lfloor kd(1+\sin\theta_0)/\pi \rfloor, \qquad n_+ = \lfloor kd(1-\sin\theta_0)/\pi \rfloor \tag{3.6}$$

define the number of propagating diffracted modes. We choose to write

$$\gamma_n = \sqrt{\beta_n^2 - k^2} \equiv -i\alpha_n \tag{3.7}$$

such that γ_n is real if $n \notin [-n_-, n_+]$. The notation and definition mimic (2.11) and we are ready to follow the methods of the previous section. Thus we define the finite Fourier transform pair

$$\bar{\phi}_n(x) = \frac{1}{2d}\int_{-d}^{d} [\phi(x,y) - \phi_{inc}(x,y)] e^{-i\beta_n y}\, dy \tag{3.8}$$

for $n \in \mathbb{Z}$ and

$$\phi(x,y) = \phi_{inc}(x,y) + \sum_{n=-\infty}^{\infty} \bar{\phi}_n(x) e^{i\beta_n y} \tag{3.9}$$

which follows from the orthogonality relation

$$\frac{1}{2d}\int_{-d}^{d} e^{i\beta_m y} e^{-i\beta_n y}\, dy = \delta_{mn}. \tag{3.10}$$

The governing wave equation is reduced to

$$\left(\frac{d^2}{dx^2} - \gamma_n^2\right)\bar{\phi}_n = 0, \qquad x \neq x_j, \ \ (j = 0, \dots, N) \tag{3.11}$$

and the transform of continuity of $\phi_x(x,y)$ at $x = x_j$ for all $y \in [-d, d]$ is expressed as

$$\frac{\partial}{\partial x}\bar{\phi}_n(x_j^+) - \frac{\partial}{\partial x}\bar{\phi}_n(x_j^-) = 0, \qquad j = 0, \dots, N. \tag{3.12}$$

Likewise, we readily find that

$$\bar{\phi}_n(x_j^+) - \bar{\phi}_n(x_j^-) = P_{n,j}, \qquad j = 0, \dots, N \tag{3.13}$$

where

$$P_{n,j} = \frac{1}{2d}\int_{-b_j}^{b_j} p_j(y) e^{-i\beta_n y}\, dy \tag{3.14}$$

and $\phi(x_j^+, y) - \phi(x_j^-, y) = p_j(y)$ for $|y| < b_j$ and is zero for $b_j < |y| < d$. With reference to the approach outlined in the previous section the transform solution can now clearly be written as

$$\bar{\phi}_n(x) = \sum_{j=0}^{N} P_{n,j} g_n(x, x_j) \tag{3.15}$$

where $g_n(x,x_j)$ satisfies (3.11), has continuous x-derivative at $x=x_j$, has a jump of unity in its value from x_j^+ to x_j^- and is outgoing at infinity for $n \in [-n_-, n_+]$ and exponentially decaying towards infinity otherwise. This gives

$$g_n(x,x_j) = -\frac{1}{2}\operatorname{sgn}(x-x_j)\mathrm{e}^{-\gamma_n|x-x_j|} \tag{3.16}$$

and so the solution in physical space is

$$\phi(x,y) = \phi_{inc}(x,y) - \frac{1}{4d}\sum_{j=0}^{N}\sum_{n=-\infty}^{\infty}\operatorname{sgn}(x-x_j)\mathrm{e}^{-\gamma_n|x-x_j|}\mathrm{e}^{\mathrm{i}\beta_n y}\int_{-b_j}^{b_j} p_j(y')\mathrm{e}^{-\mathrm{i}\beta_n y'}\,\mathrm{d}y'. \tag{3.17}$$

By comparing (3.17) to (3.2) and (3.3) in the limits $kx \to -\infty$ and $kx \to +\infty$ respectively we can deduce simply that

$$R_n = \frac{1}{4d}\sum_{j=0}^{N}\mathrm{e}^{\mathrm{i}\alpha_n x_j}\int_{-b_j}^{b_j} p_j(y')\mathrm{e}^{-\mathrm{i}\beta_n y'}\,\mathrm{d}y' \tag{3.18}$$

and

$$T_n = \delta_{n,0} - \frac{1}{4d}\sum_{j=0}^{N}\mathrm{e}^{-\mathrm{i}\alpha_n x_j}\int_{-b_j}^{b_j} p_j(y')\mathrm{e}^{-\mathrm{i}\beta_n y'}\,\mathrm{d}y' \tag{3.19}$$

for $-n_- \leqslant n \leqslant n_+$.

Coupled integral equations for the unknowns $p_j(y)$ are constructed by applying the barrier conditions (2.7) at $x = x_k$, so that

$$\frac{1}{4d}\sum_{j=0}^{N}\sum_{n=-\infty}^{\infty}\gamma_n\mathrm{e}^{-\gamma_n|x_j-x_k|}\mathrm{e}^{\mathrm{i}\beta_n y}\int_{-b_j}^{b_j} p_j(y')\mathrm{e}^{-\mathrm{i}\beta_n y'}\,\mathrm{d}y' = -\mathrm{i}\alpha_0\mathrm{e}^{\mathrm{i}\alpha_0 x_k}\mathrm{e}^{\mathrm{i}\beta_0 y}, \qquad |y| < b_k \tag{3.20}$$

and $k = 0,\ldots,N$. This equation is the analogue of (2.20) in the open domain case: infinite integrals over continuous variables β are replaced by infinite sums over discrete variables β_n. The approximation to the integral equations follows as in the previous section and the final system of equations that need to be solved in this problem remains (2.24) but with

$$K_{pq}^{(jk)} = \frac{b_j b_k}{4d}\sum_{n=-\infty}^{\infty}\gamma_n\mathrm{e}^{-\gamma_n|x_j-x_k|}D_p(\beta_n b_j)D_q(\beta_n b_k) \tag{3.21}$$

with $D_p(\lambda)$ still defined by (2.23).

It follows that

$$R_n \approx \sum_{j=0}^{N}\frac{b_j}{4d}\mathrm{e}^{\mathrm{i}\alpha_n x_j}\sum_{p=0}^{2Q+1}a_p^{(j)}D_p(\beta_n b_j), \tag{3.22}$$

and

$$T_n \approx \delta_{n,0} - \sum_{j=0}^{N}\frac{b_j}{4d}\mathrm{e}^{-\mathrm{i}\alpha_n x_j}\sum_{p=0}^{2Q+1}a_p^{(j)}D_p(\beta_n b_j), \tag{3.23}$$

for $-n_- \leqslant n \leqslant n_+$. These reflection and transmission coefficients satisfy the conservation of energy condition (see, e.g., Porter & Evans (1996))

$$E_R + E_T = 1 \quad \text{with} \quad E_R = \sum_{n=-n_-}^{n_+}\frac{\alpha_n}{\alpha_0}|R_n|^2 \quad \text{and} \quad E_T = \sum_{n=-n_-}^{n_+}\frac{\alpha_n}{\alpha_0}|T_n|^2, \tag{3.24}$$

where E_R and E_T represent total reflected and transmitted energy, respectively.

4. Arrays of partially-submerged surface-piercing barriers

In order to showcase the method further, we consider a different type of problem which is still geometrically two-dimensional. An array of $N+1$ vertical barriers are assumed to extend indefinitely and uniformly in the y-direction and, instead of extending fully through the depth of the fluid, are truncated. Thus, the barrier at $x = x_j$ occupies $-\infty < y < \infty$, and $-b_j < z < 0$, with $b_j < h$ ($j = 0, \ldots, N$), as in figure 2. We remark that b_j now denotes the full length of the plate that has previously been represented by $2b_j$ a choice made to connect with earlier sections. We retain the generality of oblique incidence of incoming surface waves and, although we can no longer trivially factorise out the depth dependence, the uniformity of the barriers in y allows us to write

$$\Phi(x, y, z, t) = \mathrm{Re}[\phi(x, z)\mathrm{e}^{\mathrm{i}\beta_0 y}\mathrm{e}^{-\mathrm{i}\omega t}], \tag{4.1}$$

where $\beta_0 = k \sin\theta_0$ is the component of the wavenumber aligned with the y-axis. Now the problem is given by

$$\left(\frac{\partial^2}{\partial x^2} + \frac{\partial^2}{\partial z^2} - \beta_0^2\right)\phi = 0 \tag{4.2}$$

with

$$\phi_z = 0, \qquad \text{on } z = -h \tag{4.3}$$

and

$$\phi_z - K\phi = 0, \qquad \text{on } z = 0 \tag{4.4}$$

along with

$$\phi_x = 0, \qquad \text{on } x = x_j^{\pm}, \quad -b_j < z < 0 \ \ (j = 0, \ldots, N). \tag{4.5}$$

Within this revised framework an obliquely-incident wave is described by the potential

$$\phi_{inc}(x, z) = \mathrm{e}^{\mathrm{i}\alpha_0 x}\psi_0(z) \tag{4.6}$$

where $\alpha_0 = k\cos\theta_0$. The conditions in the far field are

$$\phi(x, z) - \phi_{inc}(x, z) \sim \begin{cases} R\mathrm{e}^{-\mathrm{i}\alpha_0 x}\psi_0(z), & kx \to -\infty \\ (T-1)\mathrm{e}^{\mathrm{i}\alpha_0 x}\psi_0(z), & kx \to \infty \end{cases} \tag{4.7}$$

where R and T are reflection and transmission coefficients (respectively); $\phi - \phi_{inc}$ is outgoing of course. We solve the problem above by first defining orthonormal depth eigenfunctions for a domain without barriers as (e.g. Linton & McIver (2001))

$$\psi_n(z) = N_n^{-1/2}\cos k_n(z+h), \qquad N_n = \frac{1}{2}\left(1 + \frac{\sin 2k_n h}{2k_n h}\right) \tag{4.8}$$

for $n \geqslant 1$ and k_n are an increasing sequence of real positive roots of

$$K = -k_n \tan k_n h. \tag{4.9}$$

We can extend the definition to $n = 0$ by letting $k_0 = -\mathrm{i}k$ and then

$$\frac{1}{h}\int_{-h}^{0}\psi_n(z)\psi_m(z)\,\mathrm{d}z = \delta_{mn} \tag{4.10}$$

for all $m, n = 0, 1, \ldots$.

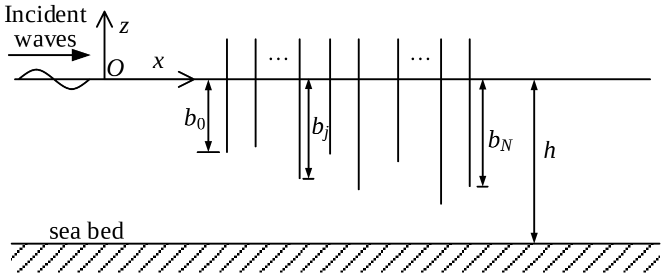

Figure 2: Sketch of wave scattering by an array of surface-piercing barriers.

We write

$$\bar{\phi}_n(x) = \frac{1}{h}\int_{-h}^{0} [\phi(x,z) - \phi_{inc}(x,z)]\psi_n(z)\,\mathrm{d}z \tag{4.11}$$

such that

$$\phi(x,z) = \phi_{inc}(x,z) + \sum_{n=0}^{\infty} \bar{\phi}_n(x)\psi_n(z) \tag{4.12}$$

follows from (4.11) and (4.10). It follows that

$$\left(\frac{\mathrm{d}^2}{\mathrm{d}x^2} - \gamma_n^2\right)\bar{\phi}_n(x) = 0, \qquad x \neq x_j, \quad (j = 0, \dots, N) \tag{4.13}$$

where, now,

$$\gamma_n = \sqrt{k_n^2 + \beta_0^2} \tag{4.14}$$

is real for $n \geqslant 1$ but, for $n = 0$, $\gamma_0 = -\mathrm{i}\alpha_0$.

We note that ϕ_x is continuous everywhere including across $x = x_j$ for all $-h < z < 0$ and so it follows that

$$\frac{\partial}{\partial x}\bar{\phi}_n(x_j^+) = \frac{\partial}{\partial x}\bar{\phi}_n(x_j^-). \tag{4.15}$$

Defining $p_j(z) = \phi(x_j^+, z) - \phi(x_j^-, z)$ which is zero for $-h < z < -b_j$ means that

$$\bar{\phi}_n(x_j^+) - \bar{\phi}_n(x_j^-) = P_{n,j} \equiv \frac{1}{h}\int_{-b_j}^{0} p_j(z)\psi_n(z)\,\mathrm{d}z \tag{4.16}$$

represents the 'depth transform' of the pressure jump across the jth barrier. With reference to the two preceding sections, we are immediately able now to write down the transform solution as

$$\bar{\phi}_n(x) = -\frac{1}{2}\sum_{j=0}^{N} P_{n,j}\operatorname{sgn}(x - x_j)\mathrm{e}^{-\gamma_n|x-x_j|} \tag{4.17}$$

(and we can confirm this satisfies all the conditions above). Thus

$$\phi(x,z) = \phi_{inc}(x,z) - \frac{1}{2h}\sum_{j=0}^{N}\operatorname{sgn}(x - x_j)\sum_{n=0}^{\infty}\mathrm{e}^{-\gamma_n|x-x_j|}\psi_n(z)\int_{-b_j}^{0} p_j(z')\psi_n(z')\,\mathrm{d}z' \tag{4.18}$$

is the general solution, expressed in terms of the unknown functions $p_j(y)$. We take the limit

$kx \to -\infty$ in the above, comparing to (4.7) to get

$$R = \frac{1}{2h} \sum_{j=0}^{N} \mathrm{e}^{\mathrm{i}kx_j} \int_{-b_j}^{0} p_j(z') \psi_0(z') \, \mathrm{d}z' \tag{4.19}$$

and

$$T = 1 - \frac{1}{2h} \sum_{j=0}^{N} \mathrm{e}^{-\mathrm{i}kx_j} \int_{-b_j}^{0} p_j(z') \psi_0(z') \, \mathrm{d}z'. \tag{4.20}$$

The unknowns $p_j(z)$ are determined by imposing the remaining no-flow conditions (4.5) on $x = x_k$ to give

$$\frac{1}{2h} \sum_{j=0}^{N} \sum_{n=0}^{\infty} \gamma_n \mathrm{e}^{-\gamma_n |x_j - x_k|} \psi_n(z) \int_{-b_j}^{0} p_j(z') \psi_n(z') \, \mathrm{d}z' = -\mathrm{i}\alpha_0 \mathrm{e}^{\mathrm{i}\alpha_0 x_k} \psi_0(z), \qquad -b_k < z < 0 \tag{4.21}$$

for $k = 0, \ldots, N$. The coupled integral equations are solved using the method first described in Porter & Evans (1995) in which

$$p_j(z) \approx \sum_{p=0}^{Q} a_p^{(j)} w_p(z/b_j) \tag{4.22}$$

and

$$\hat{w}_p(u) = w_p(u) - Kb_j \int_{-1}^{u} w_p(s) \, \mathrm{d}s \tag{4.23}$$

where

$$\hat{w}_p(u) = \frac{2(-1)^p}{(2p+1)\pi} \sqrt{1-u^2} \mathrm{U}_{2p}(u) \tag{4.24}$$

is designed to ensure that the free surface condition (4.4) is satisfied as well as retaining the correct local square-root behaviour of the pressure jump in the vicinity of the lower edge of the plates. It follows that (Porter & Evans 1995)

$$D_{np}^{(j)} = \int_{-b_j}^{0} \psi_n(z) w_p(z/b_j) \, \mathrm{d}z = N_n^{-1/2} \cos(k_n h) \int_{-b_j}^{0} \cos(k_n z) \hat{w}_p(z/b_j) \, \mathrm{d}z \tag{4.25}$$

after integrating by parts, is given by

$$D_{np}^{(j)} = N_n^{-1/2} \cos(k_n h) \mathrm{J}_{2p+1}(k_n b_j)/(k_n b_j) \tag{4.26}$$

which, for $n = 0$, is better expressed as

$$D_{0p}^{(j)} = (-1)^p N_0^{-1/2} \cosh(kh) \mathrm{I}_{2p+1}(kb_j)/(kb_j) \tag{4.27}$$

where $\mathrm{I}_p(\cdot)$ is a modified Bessel function of the first kind of order p. Substituting (4.22) into (4.21), and multiplying through by $w_q(z/b_k)$ before integrating over $-b_k < z < 0$ gives the system of equations

$$\sum_{j=0}^{N} \sum_{p=0}^{Q} a_p^{(j)} K_{pq}^{(jk)} = -\mathrm{i}\alpha_0 \mathrm{e}^{\mathrm{i}\alpha_0 x_k} D_{0q}^{(k)}, \qquad k = 0, \ldots, N, \; q = 0, \ldots, Q. \tag{4.28}$$

where

$$K_{pq}^{(jk)} = \frac{b_j b_k}{2h} \sum_{n=0}^{\infty} \gamma_n e^{-\gamma_n |x_j - x_k|} D_{np}^{(j)} D_{nq}^{(k)}. \tag{4.29}$$

For $j \neq k$ the series is exponentially-convergent. When $j = k$, the series defining $K_{pq}^{(jj)}$ resembles that encountered in Porter & Evans (1995) for a plate in isolation in which terms decay like $O(1/n^2)$. It is possible to accelerate the convergence of the series defining $K_{pq}^{(jj)}$ by subtracting the leading-order asymptotic behaviour of each term in the series which can be deduced from $k_n h \sim n\pi$, $N_n \sim \frac{1}{2}$, $\gamma_n h \sim n\pi$ as $n \to \infty$. The infinite series which compensates for the subtraction can then be evaluated as a different infinite series (see Paris (2018)) which, for the present purposes, is not worth pursuing.

In the case that plates are positioned at regular intervals, $x_j = jc$, with spacing c and submerged to the same depth, $b_j = b_0 = b$, which corresponds to the case considered by Huang & Porter (2023) then

$$K_{pq}^{(jk)} = \frac{b^2}{2h} \sum_{n=0}^{\infty} \gamma_n e^{-\gamma_n |j-k| c} D_{np}^{(0)} D_{nq}^{(0)} \tag{4.30}$$

depends only on $|j-k|$ and only needs $N+1$ evaluations for $|j-k| = 0, \ldots, N$.

Using (4.22) in (4.19) and (4.20) gives

$$R \approx \sum_{j=0}^{N} \frac{b_j}{2h} e^{ikx_j} \sum_{p=0}^{Q} a_p^{(q)} D_{0p}^{(j)} \tag{4.31}$$

and

$$T \approx 1 - \sum_{j=0}^{N} \frac{b_j}{2h} e^{-ikx_j} \sum_{p=0}^{Q} a_p^{(q)} D_{0p}^{(j)} \tag{4.32}$$

and these coefficients should satisfy $|R|^2 + |T|^2 = 1$.

5. Results in open domain

5.1. *A circular cylinder*

We first consider the scattering of waves by a circular metacylinder, as first studied by Zheng *et al.* (2020) and later by Putley *et al.* (2022). Both used homogenisation to replace the discrete plate array with an effective medium. The present work allows us to validate the numerical method described in this paper by demonstrating convergence to the homogenisation results as N, the number of plates in the discrete array, increase. Figure 3 depicts the scattering energy σ, defined in (2.36), as a function of the nondimensional wavenumber ka under the oblique wave excitation ($\theta_0 = 45°$), where a denotes the radius of the metacylinder. We present curves associated with metacylinders having $N = 10$, 15, and 20 channels of constant width which can be seen to converge to the results of Zheng *et al.* (2020) (the homogenisation results have been obtained by truncating their numerical system of equations at 20 terms) as N increases for $ka < \pi/2$. The vertical line corresponds to $ka = \pi/2$ which signals the onset of fluid resonance in narrow channels and the homogenisation method fails for ka beyond this value (Putley *et al.* 2023). Our method therefore allows us to consider results for $ka > \pi/2$. A general observation is that larger N are required for convergence as the frequency increases and that the scattering energy generally increases with the wavenumber and exhibits oscillations near integer multiples of $\pi/2$, representing the onset of new gap resonance modes

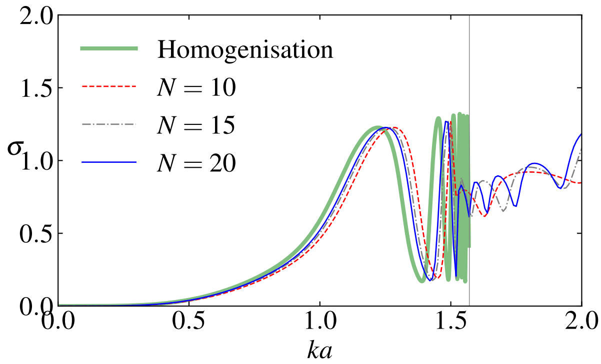

Figure 3: Scattering energy σ by circular metacylinders with different number of channels N under the quartering wave excitation $\theta_0 = 45°$ as a function of nondimensional wavenumber ka. Comparison is made with the homogenisation solution by Zheng *et al.* (2020) which is valid when $ka < \pi/2$.

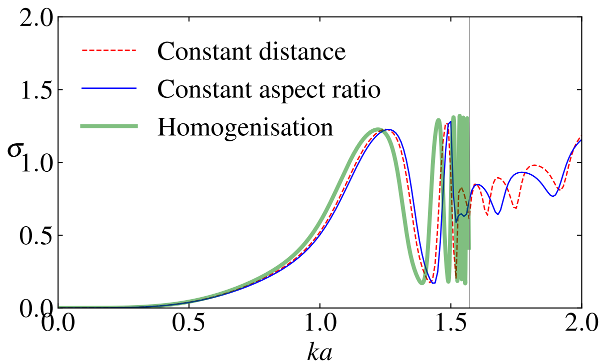

Figure 4: Comparison of scattering energy by circular metacylinders composed of $N = 20$ channels for different plate separation constrained by constant channel aspect ratio and equal spacing. Comparison is made with the homogenisation solution valid for $ka < \pi/2$.

in the central channel (Molin *et al.* 2002). It is noteworthy that the wavenumbers $ka = n\pi/2$ with $n \in \mathbb{Z}^+$ for gap resonance in the central channel are determined by the assumption of homogeneous Dirichlet conditions $\phi = 0$ at the ends of the channel. However, this assumption holds true only if the gap width is very small (Liang *et al.* 2023).

In figure 4 we compare the results of figure 3 for $N = 20$ channels of uniform width with a distribution the plates within the metacylinder which maintains a constant aspect ratio of channel width to (mean) length. This new scheme therefore concentrates plates towards the two extremes of the cylinder. Although there are only small differences, the uniform width case is found to marginally improve convergence to the $N = \infty$ limit.

This observation is made clearer in figure 5 where a comparison of the effect of plate distribution and the value of N on the free surface is presented. A wave incident from $\theta_0 = 45°$ at frequencies determined by $ka = 1$ (left column), 2 (middle) and 3 (right). In the first and third rows, the channel spacing is uniform and there are $N = 10$, $N = 20$ channels, respectively. In the second and fourth rows $N = 10$, $N = 20$ once again but the plate distribution maintains constant channel aspect ratio. The final row shows results from homogenisation. Note that the final two results for $ka = 2$, $ka = 3$ are invalid since there is resonance inside the cylinder which violates the homogenisation assumptions. The plot shows more significant differences in the results for different spacing schemes at higher frequencies. We also note the presence of large local resonance within the cylinder, and the wave amplitude displayed is chopped to 2.0.

5.2. *Rectangular and graded metawedge*

As a sequel to the study on circular metacylinders, we now investigate wave scattering by metarectangles and graded metawedges, which have been less explored in the literature. Figure 6 presents the instantaneous wave patterns at $t = 0$ scattered by a metarectangle for different aspect ratios, including AR = 1.0 and AR = 5.0, shown in the top and bottom rows, respectively. Here, the aspect ratio (AR) is defined as the ratio of the length to the width of the metarectangle. Wave patterns for $kb = \pi/2$ and $kb = \pi$ are presented in the left and right columns.

For the metasquare (AR = 1.0), shown in the top row, the symmetrical property with respect to $y = x$ is disrupted due to the presence of channels. Notably, wave trapping in the channel on the upwave side is observed at $kb = \pi$. In the case of an elongated metarectangle (AR = 5.0), depicted in the bottom row, large free surface responses are observed in the first channel facing the wave incidence. Besides, there is a noticeable wave twisting within the metarectangle, similar to the phenomenon described by Porter (2021) for an infinite setting. Unlike the perfect transmission reported in Porter (2021), however, the presence of end effects leads to appreciable disturbances riding on the wave crest/trough.

In figure 7, we consider the diffraction energy σ under the normal wave incidence $\beta = 0°$ for a metasquare and a metawedge, depicted in the left and right panels, respectively. Here we define the base ratio of the metawedge as $\ell = b_N/b_0$, and the mean semiwdith $b_m = (b_0 + b_N)/2$. When the base ratio is unequal to unity $\ell \neq 1$, the constant aspect ratio separation strategy is employed in the configuration of the metawedge. The results show a good agreement between the two alternative representations provided by Eq. (2.36), thereby confirming the accuracy of the computation. In both cases, the scattering energy exhibits a step-shaped increase. For the metasquare, depicted in the left subplot, strong oscillations occur at the beginning of the step. Although the metawedge, shown in the right subplot, also exhibits fluctuations in the scattering energy, the oscillation amplitude is much smaller.

Figure 8 illustrates the free surface elevation along the center line of the metasquare ($\ell = 1$) and metawedge ($\ell = 3$), shown in the left and right panels, respectively, as a function of the normalised wavenumber kb_m ranging from 0 to 10. The white lines indicate the locations of the plates, and the layout is identical to the setup in figure 7.

Within the metastructure, significant wave trapping accompanied by large-amplitude wave responses is observed – see figure 9. For the metasquare, wave trapping occurs at discrete frequencies, whereas for the metawedge, waves are trapped over a broad range of frequencies, demonstrating a "rainbow reflection" behaviour. In both cases, the downwave side of the metastructure experiences minimal disturbance, exhibiting shielding effects; see figure 8 for $x > b_m$. Notably we see from figure 8 that the metawedge provides superior shielding effects compared to the metasquare because of rainbow reflection, resulting in a larger quiet region over a wide range of frequencies.

6. Results for periodic arrays

Following the physical findings of wave scattering by a single metastructure in open domain considered in § 5, our focus now turns to the analysis of periodic array scenarios as studied in § 3. Specifically, we aim at delving into the underlying physics of wave patterns associated

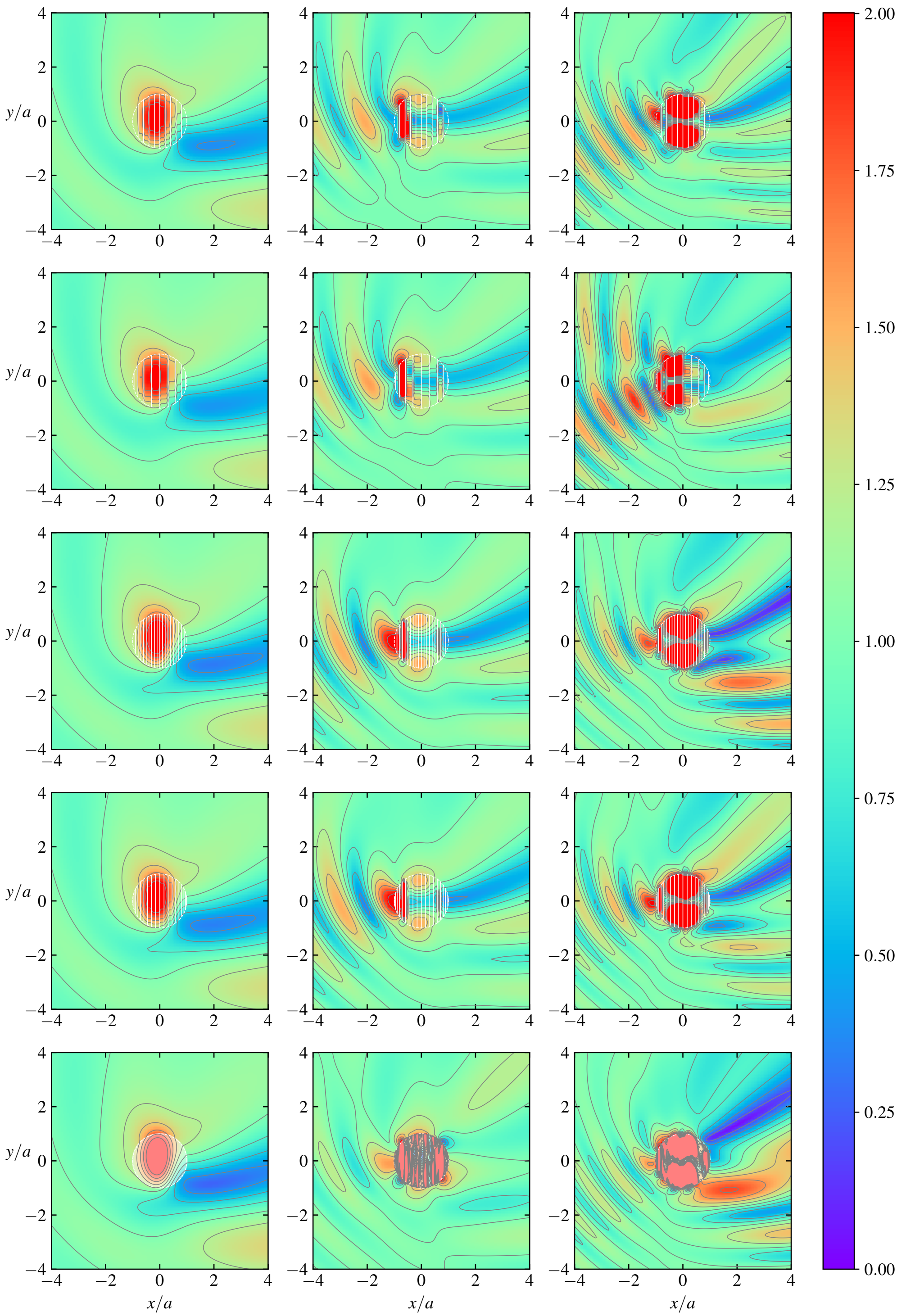

Figure 5: Modulus of wave patterns scattered by a circular metacylinder for different number of plates and separation strategies. The wave patterns associated with 10 channels uniform spacing (top row), 10 channels constant aspect ratio (second row), 20 channels uniform spacing (third row), 20 channels constant aspect ratio (fourth row), and homogenisation solution (bottom row) are exhibited for $ka = 1.0$ (left), 2.0 (middle) and 3.0 (right).

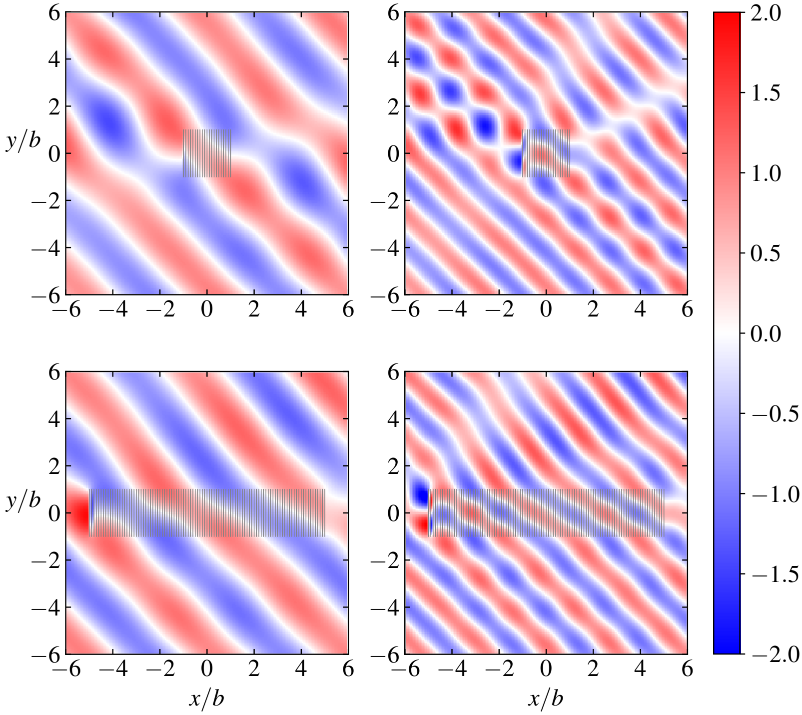

Figure 6: Instantaneous wave patterns at $t = 0$ scattered by a rectangular metacylinder for different aspect ratios at $kb = \pi/2$ (left) and $kb = \pi$ (right). The top, middle and bottom rows show the results for AR = 1.0 and 5.0, respectively.

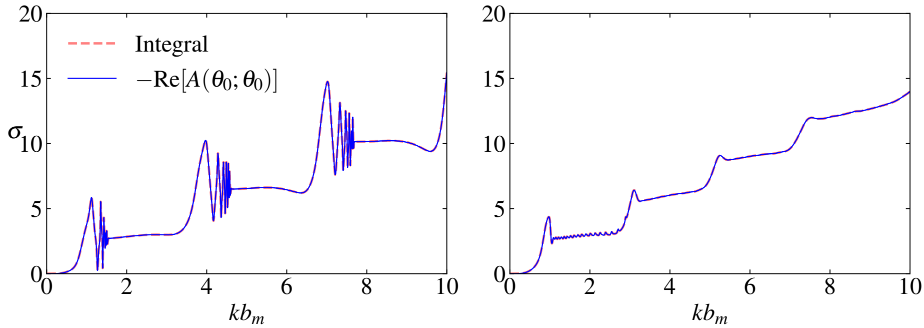

Figure 7: Scattering energy σ under the normal wave excitation ($\beta = 0°$) as a function of non-dimensional wavenumber kb_m for base ratios $\ell = 1$ (left panel, metasquare) and $\ell = 3$ (right panel, metawedge).

with nearly total reflection and nearly perfect transmission, as predicted by the energy relation given by (3.24).

6.1. *Circular metacylinder*

We first study the scattering of waves by a periodic array of circular metacylinders. Figure 10 illustrates the reflection energy E_R, defined in (3.24), by a periodic array of circular metacylinders as a function of the nondimensional wavenumber ka, where a represents the radius of metacylinder. Both normal incidence ($\theta_0 = 0°$) and oblique incidence ($\theta_0 = 45°$)

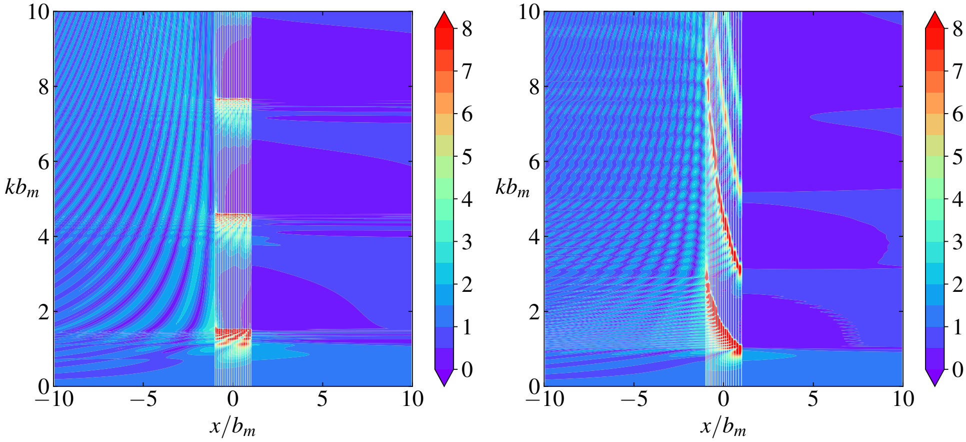

Figure 8: Free surface elevation along the centre line of the metasquare $\ell = 1$ (left) and metawedge $\ell = 3$ (right) varying with the normalised wavenumber kb_m.

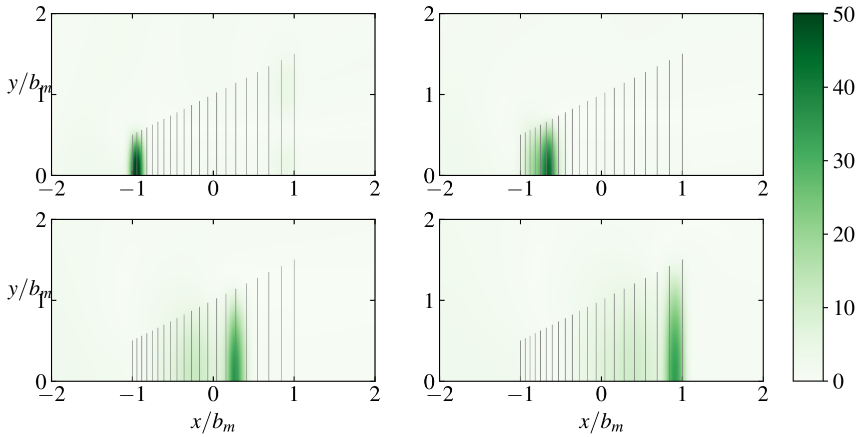

Figure 9: Demonstration of rainbow trapping in the 1st, 6th, 16th and 20th channels at $kb_m = 2.90, 2.25, 1.35, 1.02$, respectively. The colourbar indicates the modulus of free surface elevation.

are presented, displayed in the left and right subplots, respectively. In this configuration, half the centre-to-centre distance between adjacent metacylinders is twice the radius ($d = 2a$). In this setup, the lowest resonant wavenumber $ka = \pi/2$ in the metacylinder coincides with the crossing mode wavenumber $kd = \pi$.

In the left subplot depicting normal incidence, we observe a sharp transition in the reflection energy. As the wavenumber approaches $ka = \pi/2$, the reflection changes from nearly-perfect transmission ($E_R \to 0$) to nearly-total reflection ($E_R \to 1$) occurred at $ka \approx 1.5036$ and $ka \approx 1.5707$, respectively. On the other hand, under oblique wave excitation, as in the right subplot, there exists specific wavenumbers where reflection is inconsequential, whereas complete reflection does not occur in this setup.

To further elucidate the underlying physics governing the phenomena of nearly total transmission and nearly perfect reflection described in figure 10, we examine the free surface responses at these wavenumbers.

Figure 11 presents the wave patterns scattered by a circular metacylinder under the action

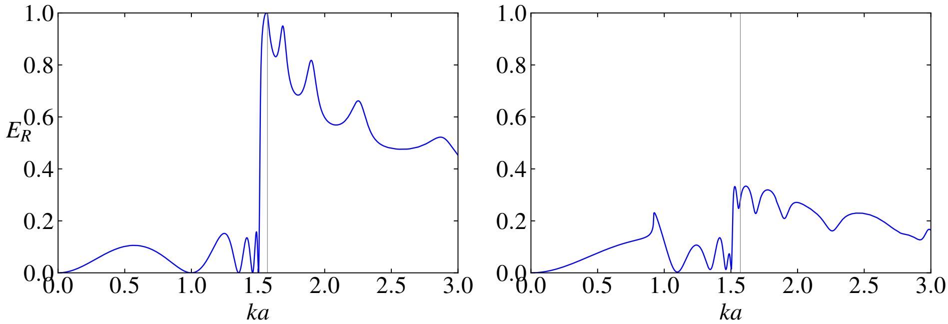

Figure 10: Reflection energy for a periodic array of circular metacylinders with $a/d = 0.5$ for $\theta_0 = 0°$ (left) and $\theta_0 = 45°$ (right). The vertical line corresponds to $ka = \pi/2$, where a denotes the radius of the circular metacylinder.

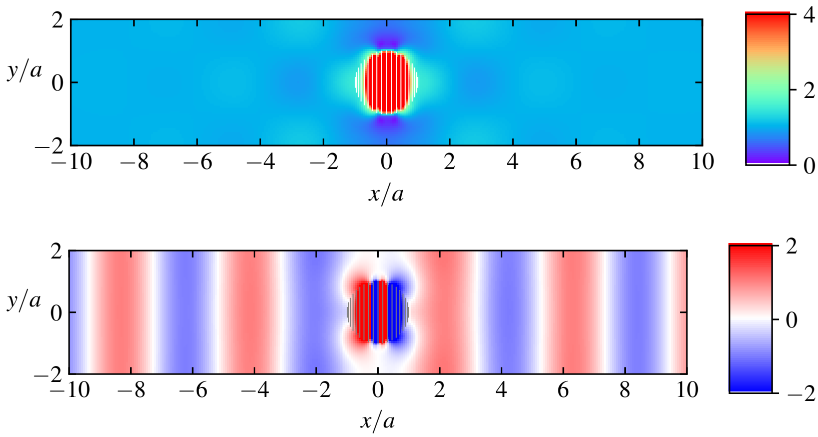

Figure 11: Wave patterns scattered by a periodic array of circular metacylinders under normal wave incidence ($\theta_0 = 0°$) at $ka = 1.5036$ with a normalised radius of $a/d = 0.5$, illustrating nearly perfect wave transmission. The top and bottom subplots exhibit the modulus and real part of the wave pattern, respectively.

of normal incidence ($\theta_0 = 0°$) at $ka = 1.5036$ corresponding to nearly total transmission. The top and bottom subplots show modulus and instantaneous wave patterns, respectively. It is notably observed that that waves are trapped within the gaps of the plate arrays constituting the circular metacylinder, resulting in large free surface responses. Furthermore, at significant distances from the metacylinder, the wave field maintains the profile of the incident waves, indicating the occurrence of perfect transmission.

Figure 12 illustrates the diffraction wave field at $ka = 1.5707$ under the head wave excitation $\theta_0 = 0°$, at which waves are nearly totally reflected. On the downwave side, however, the flow field still remains disturbed, and the crossing mode $\cos(\pi y/d)$ is predominant exhibiting standing wave behaviours. Considering the wavenumber $ka = 1.5707$, slightly less than $\pi/2$, it can be expressed as $kd = 2ka = \pi - \epsilon$, where $\epsilon \ll 1$. The characteristic wavenumber γ_1 is approximated as:

$$\gamma_1 = \sqrt{\pi^2/d^2 - (\pi - \epsilon)^2/d^2} \approx \sqrt{2\epsilon\pi/d^2}. \tag{6.1}$$

The smallness of the characteristic wavenumber γ_1 leads to a slow decay of the associated

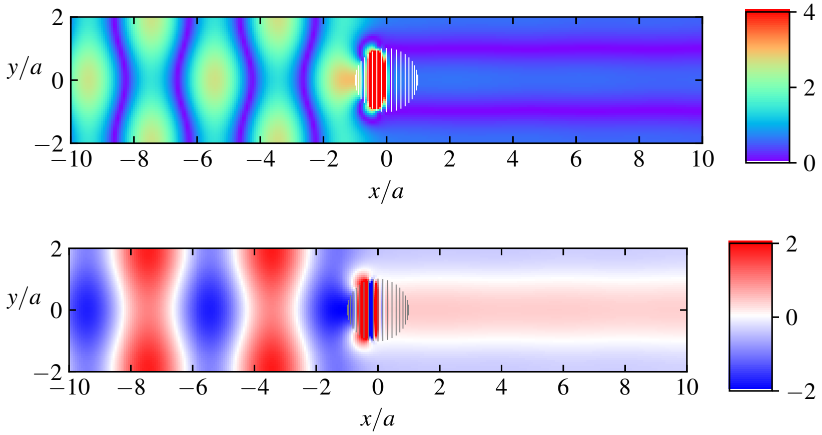

Figure 12: Wave patterns scattered by a periodic array of circular metacylinders with a normalised radius of $a/d = 0.5$ under normal wave incidence ($\theta_0 = 0°$) at $ka = 1.5707$ close to crossing mode wavenumber $ka = \pi/2$, exhibiting nearly total reflection. The top and bottom subplots exhibit the modulus and real part of the wave pattern, respectively.

evanescent mode. Although this mode will eventually diminish at a significant distance from the metacylinder, it persists within a fairly large region surrounding the metacylinder.

In the case of oblique wave excitation, we focus on the wavenumber $ka = 1.5025$, characterised by minimal energy reflection. Figure 13 showcases the wave patterns scattered by a periodic array of circular metacylinders at $ka = 1.5025$, where the energy reflection is minimal, leading to nearly total transmission. Notably, the transmitted waves propagate at a different angle compared to the incident waves. Specifically, at $ka = 1.5025$, the far-field transmitted waves are dominated by the components T_{-1} and T_0, with $|T_{-1}| > |T_0|$. As a consequence, the propagation of transmitted waves is primarily governed by the angle $\theta_{-1} = \arctan(\beta_{-1}/\alpha_{-1}) \approx -19.78°$. Therefore, if the component T_0 is smaller than other components, the transmitted waves will propagate at an angle different from the incident waves, resulting in wave bending effects. This feature of metagratings was also discussed by (Putley *et al.* 2022).

6.2. *Metasquare*

We turn our attention to wave scattering by a periodic array of metasquares, where the plate width is $b/d = 0.5$. Figure 14 depicts the variation of reflection energy E_T with respect to the nondimensional wavenumber kb considering both head wave incidence ($\theta_0 = 0°$) and oblique wave incidence ($\theta_0 = 45°$) displayed in the left and right subplots, respectively. Under the normal wave incidence as in the left subplot, the reflection energy experiences strong oscillations near $kb = \pi/2$, rapidly alternating between total transmission and perfect reflection. The same oscillatory behaviours were also observed in the scattering of acoustic wave by a rectangular metamaterial cavity (Jan & Porter 2018) due to complex interference. In the oblique wave excitation as in the right subplot, the strong oscillations near $kb = \pi/2$ are also observed, and there exist a dense discrete wavenumbers at which the nearly perfect wave transmission occurs. However, the value of reflection energy E_R does not exceed 0.5 within the considered wavenumber range, and thus perfect reflection is not achieved.

To illustrate the total reflection $E_R \to 1$ under the normal wave incidence by a metasquare, we examine the wave patterns at $kb = 1.5350$, where the wave transmission is minimised, as shown in figure 15. Unlike the scenario of perfect reflection by a periodic array of circular

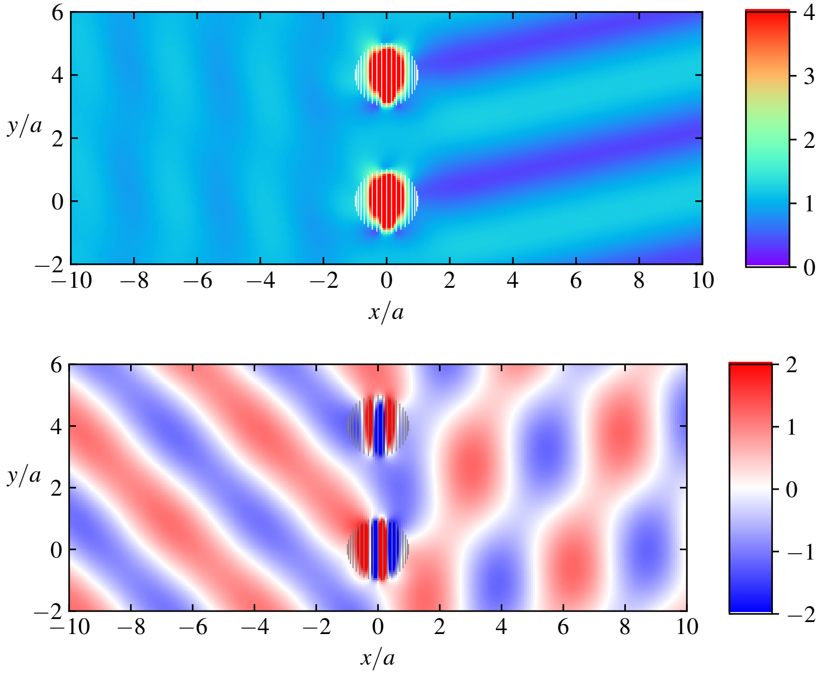

Figure 13: Wave pattern scattered by a periodic array of circular metacylinders with a normalised radius $a/d = 0.5$ under the oblique wave excitation ($\theta_0 = 45°$) at a wavenumber $ka = 1.5025$, showing nearly perfect wave transmission and wave bending effects on the downwave side.

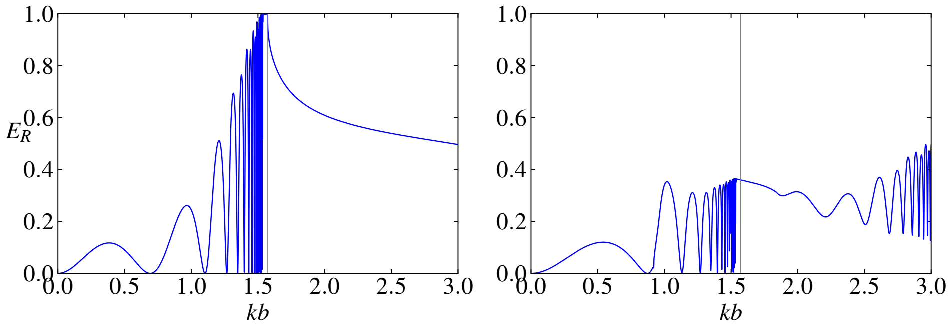

Figure 14: Reflection energy for a periodic array of metasquares with $b/d = 0.5$ under head wave incidence $\theta_0 = 0°$ (left) and oblique incidence $\theta_0 = 45°$ (right). The vertical line corresponds to $kb = \pi/2$, where b denotes semi-width of the plate constituting the metasquare.

metacylinders in figure 12, where the wavenumber $ka = 1.5707$ closely aligns with the crossing mode wavenumber $ka = \pi/2$, the current wavenumber deviates from the crossing mode wavenumber. As a consequence, the evanescent mode, associated with the characteristic wavenumber γ_1, decays rapidly with distance from the metasquare, resulting in a quiescent flow field on the downwave side of the structure.

To showcase the perfect wave transmission predicted by the reflection energy plot, shown in the right subplot of figure 14, for the scattering of an array of metasquares by oblique

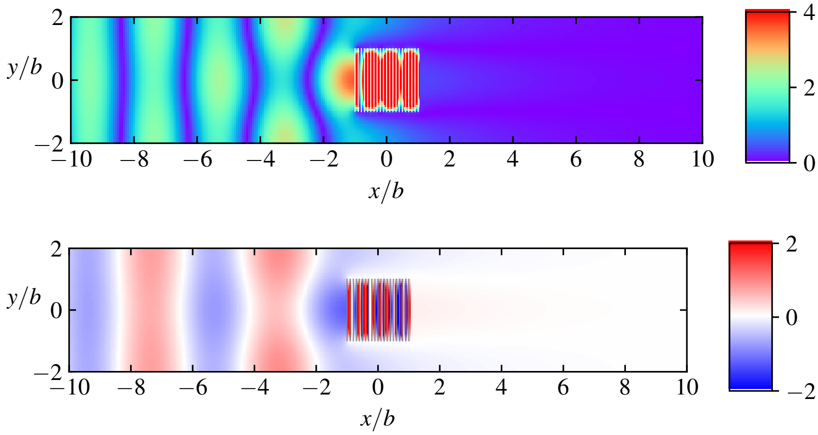

Figure 15: Wave pattern scattered by a periodic array of metasquares with a semi-width ratio of $b/d = 0.5$, under head wave excitation ($\theta_0 = 0°$) at $kb = 1.5350$, illustrating nearly total wave reflection. The top and bottom subplots exhibit the modulus and real part of the wave pattern, respectively.

waves ($\theta_0 = 45°$), wave patterns at a wavenumber $kb = 1.3975$ are presented in figure 16. It is observed that the upwave flow field is minimally disturbed, indicating nearly perfect transmission of wave energy. Additionally, the wave field downstream aligns closely with the incident wave pattern, different from the scenario of oblique wave interactions with an array of circular metacylinders shown in figure 13, where wave propagation bends. In the current setup, however, the transmitted wave associated with T_0 predominates over the component with T_{-1}, i.e., $T_0 \gg T_{-1}$. Therefore, wave propagation remains unchanged, with only a phase shift occurring.

6.3. *Metawedge*

For a periodic array of metawedges, we consider the setup with an averaged semi-width of $b_m/d = 0.5$ and a ratio of longer base to shorter base $\ell = 3.0$. Figure 17 presents the reflection energy under the head wave incidence ($\theta_0 = 0°$) and oblique wave incidence ($\theta_0 = 45°$), displayed in the left and right subplots, respectively. One notable feature in the left subplot is the nearly total reflection of waves across a wide spectrum of wavenumbers, indicating that the device can act as a 'broadband wave reflector'. Under the quartering wave excitation as in the right subplot, neither total wave reflection nor perfect wave transmission occurs within the considered range of wavenumbers.

To illustrate the near-perfect reflection achieved by the metawedge array, figure 18 presents the modulus, real part, and imaginary part of the wave pattern corresponding to $kb_m = 1.1980$ under head sea excitation. The setup of the metawedge is identical to the one considered in figure 17. In this case, the wave energy experiences complete reflection resulting in a quiet flow field on the downwave side. On the upwave side, the real part is predominant whereas the imaginary part is negligible. As a consequence, the wave pattern on the upwave side manifests standing wave characteristics. Moreover, the wave crestlines are straight except the flow region in the vicinity of the metawedge, then exhibiting two dimensional behaviours.

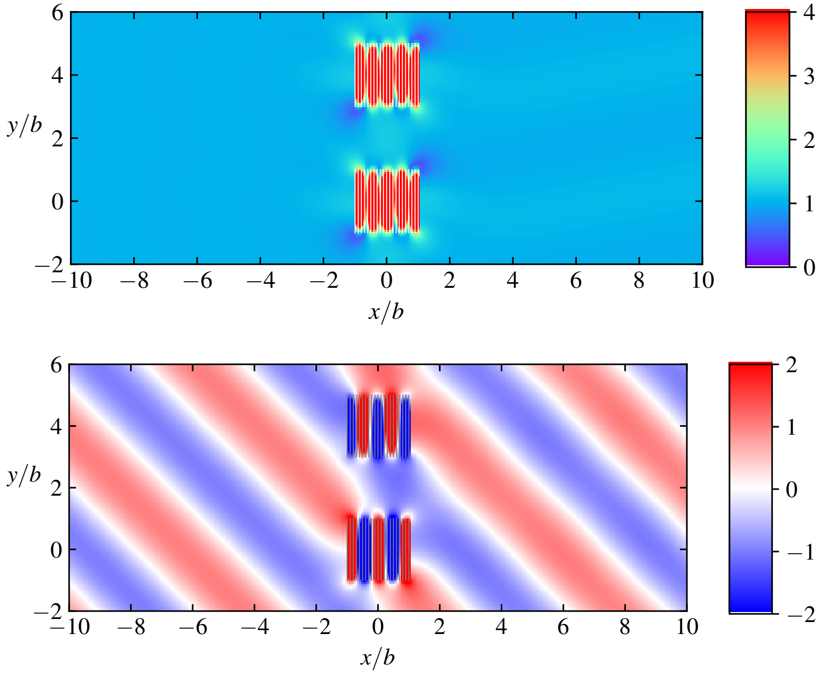

Figure 16: Wave pattern scattered by a periodic array of metasquares with a semi-width ratio of $b/d = 0.5$, under the action of oblique waves ($\theta_0 = 45°$) at $kb = 1.3975$, illustrating nearly perfect wave transmission. The top and bottom subplots exhibit the modulus and real part of the wave pattern, respectively.

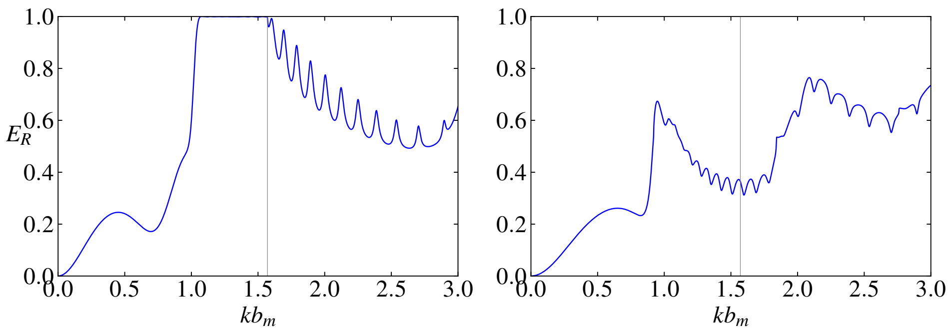

Figure 17: Reflection energy for a periodic array of metawedges with the averaged semi-width $b_m/d = 0.5$ and base ratio $\ell = 3.0$ under the actions of head waves $\theta_0 = 0°$ (left) and oblique waves $\theta_0 = 45°$ (right). The vertical line corresponds to $kb_m = \pi/2$.

7. Results for surface-piercing plate-arrays

Finally, we investigate the scattering of waves by an array of two-dimensional partially-submerged surface-piercing barriers.

7.1. *Verification*

For verification purposes, we show in figure 19 the modulus of the reflection coefficient, $|R|$, for an array of vertical barriers with uniform truncated depth b. The results presented on the left and right side of the figure correspond to a gap width of $c/b = 0.5$ and $c/b = 0.05$, and

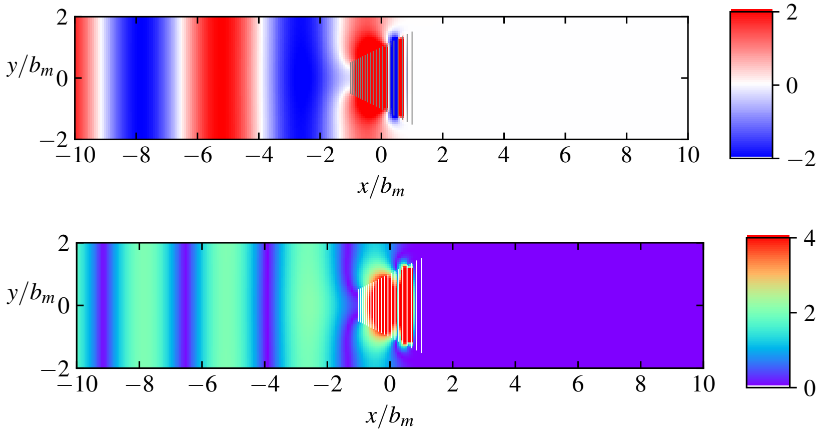

Figure 18: Wave pattern scattered by a periodic array of metawedges, with an averaged semi-width of $b_m/d = 0.5$ and longer-to-shorter base ratio $\ell = 3$, under the excitation of head waves ($\theta_0 = 0°$) at $kb_m = 1.1980$ illustrating nearly perfect reflection. The top and bottom subplots exhibit the modulus and real part of the wave pattern, respectively.

the top and bottom rows exhibit the results for $N = 1$ and $N = 10$ cavities, respectively. Good agreement is made with the solutions obtained from the discrete model developed in Huang & Porter (2023).

In the case of a single cavity, depicted in the top row, the reflection coefficient experiences a transition from total transmission $|R| = 0$ to perfect reflection $|R| = 1$. This transition becomes sharp as the cavity gap c/b decreases, and it occurs in the vicinity of the resonance frequency $\omega \approx \sqrt{g/b}$ corresponding to $Kb \approx 1$ (Newman 1974). For multiple cavities as shown in the bottom row the solution exhibits increasingly rapid oscillations as the frequency approaches the resonant frequency for a single cavity and practically no transmission for frequencies beyond. As discussed in Huang & Porter (2023), oscillations arise from constructive/destructive interference effects from the ends of the array compounded with a retardation of the effective wave speed through the array (exemplified in figure 21) as resonance is approached.

7.2. *Uniform and graded plate-arrays*

We continue by making a comparison between uniform arrays of Huang & Porter (2023) and the graded arrays considered in Wilks *et al.* (2022). Figure 20 presents reflection coefficient $|R|$ for both uniform and graded surface-piercing plate-arrays under normal wave incidence ($\theta_0 = 0°$). The metastructure is composed of $N = 20$ cavities, spanning the interval $x/h \in [-0.5, +0.5]$, with an average plate immersion of $b_m/h = 0.5$. For the graded plate-array, we adopted a constant aspect ratio strategy, with a base length ratio of $b_N/b_0 = 3.0$.

As already described, $|R|$ for the uniform plate-array exhibits rapid oscillations between $|R| = 0$ and peaks approaching $|R| = 1$ at resonance. The region of strong oscillations is magnified in the right panel. In contrast, the reflection curve for the graded plate-array is smooth, free of oscillatory behaviours, transitioning to $|R| = 1$ at $Kb_N = 1$, corresponding to $Kb_m = 2/3$ plotted by the gray vertical line in the figure.

Figure 21 exhibits the imaginary part of spatial potential distribution $\mathrm{Im}[\phi(x,z)]$ within the flow field for wave scattering by a surface-piercing plate-array. The top and middle panels illustrate potential distribution for a uniform plate-array at $Kb_m = 0.977698$ and $Kb_m = 0.978375$, respectively. Despite slight variation in wavenumber, the reflection coefficient

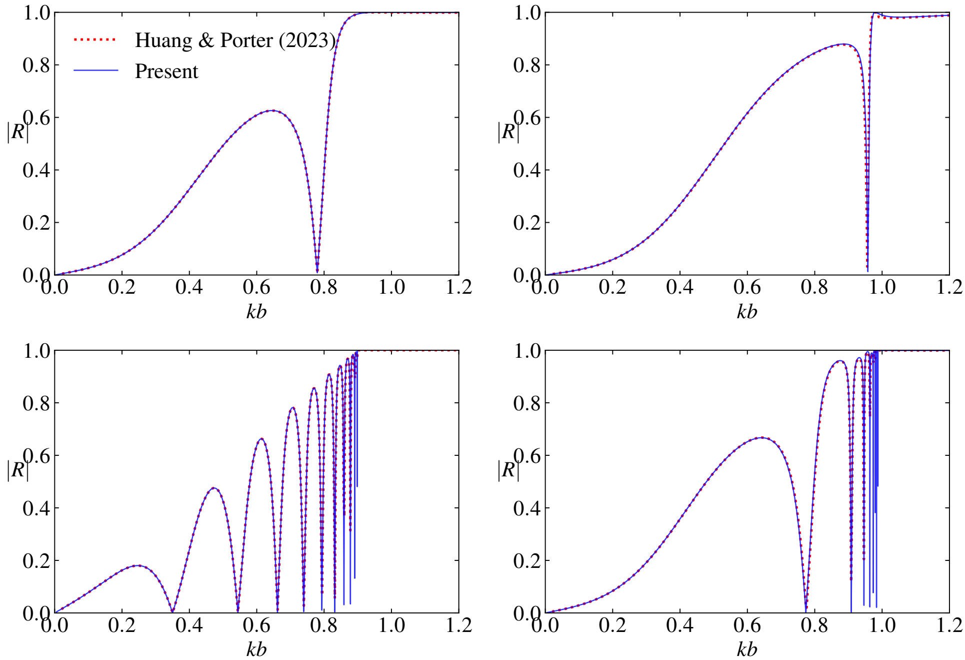

Figure 19: Modulus of the reflection coefficient $|R|$ by an array of vertical identical barriers for gaps $c/b = 0.5$ (left) and $c/b = 0.05$ (right) at $b/h = 0.2$, where c denotes the distance between adjacent barriers and b is the truncated depth. Top and bottom rows are for $N = 1$ and $N = 10$ cavities, respectively. Comparison is made with the discrete model by Huang & Porter (2023).

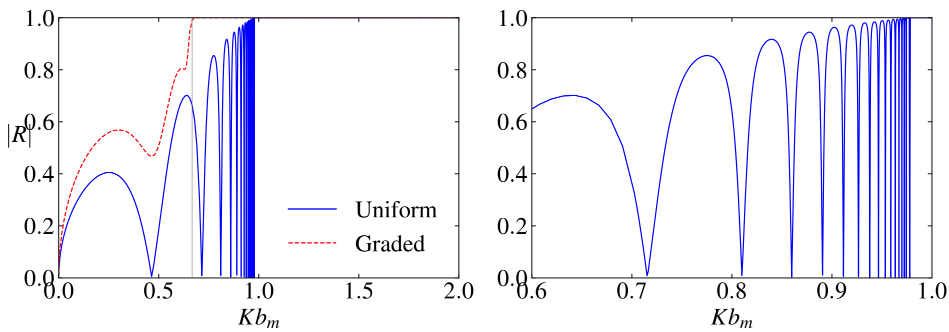

Figure 20: The modulus of the reflection coefficient $|R|$ by an array of uniform and graded vertical barriers for $\theta_0 = 0°$ with the right panel highlighting the area where the reflection curve for the uniform array touch the zero. The vertical gray line at $Kb_m = 2/3$ corresponds to the lowest resonant wavenumber for the graded plate-array over which perfect reflection occurs.

undergoes a sharp transition from $|T| = 0$ to $|T| = 1$ corresponding to complete transmission and perfect reflection, respectively, indicating a dramatic shift in the flow field dynamics. The top panel shows a multiple interference effect from the ends of the array with large fluid response within the cavities and the middle panel shows an exponential decay through the array. In contrast, the bottom panel exhibits the scenario where the plate-array is graded, where perfect reflection is observed for all $Kb_m \gtrsim 0.66$. In this configuration a wave is

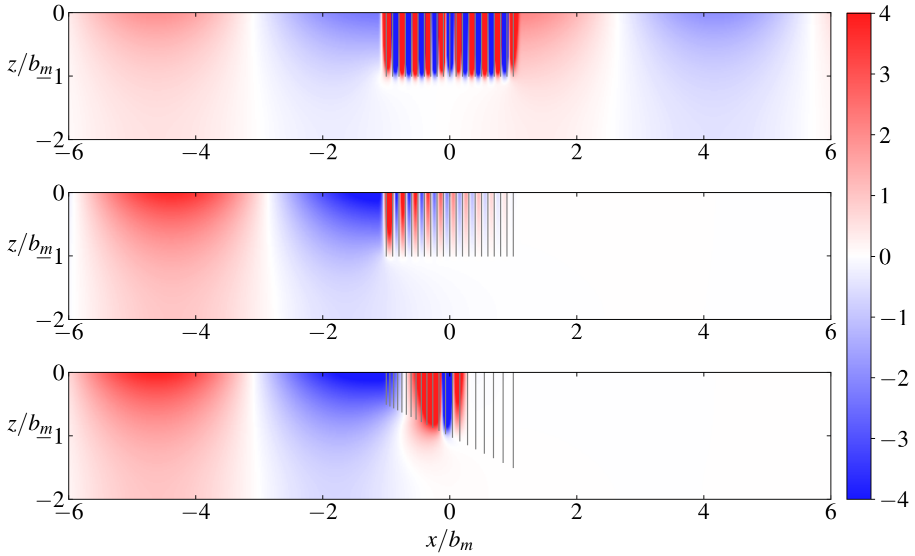

Figure 21: Distribution of the imaginary part of the velocity potential in the flow field for wave scattering by a surface-piercing plate-array under normal incidence $\theta_0 = 0°$. Top: uniform plate-array at $Kb_m = 0.977698$; middle: uniform plate-array at $Kb_m = 0.978375$; bottom: graded plate-array at $Kb_m = 0.977698$.

trapped within the middle cavity where the group velocity has slowed to zero and hardly any fluid motion is observed downwave of this.

The theory developed in the paper allows for oblique wave incidence, but we found that the results did not change too much in character after replacing k by $k\cos\theta_0$, being the x-component of the wavenumber.

7.3. *Semi-circular plate-array*

Finally we consider the wave scattering by a semi-circular profiled plate-array. Figure 22 depicts the reflection curve as a function of non-dimensional wavenumber ka, where a denotes the radius of the semi-circle. This is also a graded array with the onset of resonance associated with the longest channel, therefore at $Ka = 1$. We observe a similar type of behaviour in $|R|$ and the plot for the potential field as for graded arrays. That is, we transition to $|R| = 1$ for $Ka > 1$ preceded by a small number of oscillations in the reflection before $Ka = 1$; and the fluid motion dies downwave of the cavity at which resonance occurs.

Similar as figure 21, figure 23 presents the imaginary components of the potential distribution, $\mathrm{Im}[\phi(x, z)]$, within the flow field for wave scattering by a semi-circular profiled plate array. The top and bottom panels illustrate the cases of total transmission and perfect reflection at $Ka = 0.958022$ and $Ka = 1.092743$, respectively, corresponding to $|R| = 0$ and $|R| = 1$ as in figure 22. Due to the graded nature of the semi-circular metastructure, the physical properties are analogous to those of the wedge-shaped plate-array.

8. Conclusions

In this paper we have considered a variety of settings in which water waves interact with metastructures consisting of dense plate arrays. These settings include the scattering of plane waves by isolated vertical metacylinders extending uniformly through the depth in an open ocean, scattering of plane waves by periodic arrays of vertical metacylinders and oblique

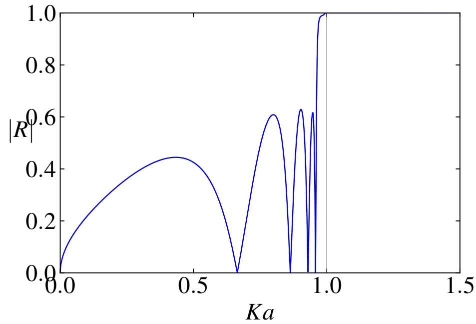

Figure 22: The modulus of the reflection coefficient $|R|$ by an array of vertical barriers subject to semi-circular profile for $\theta_0 = 0°$.

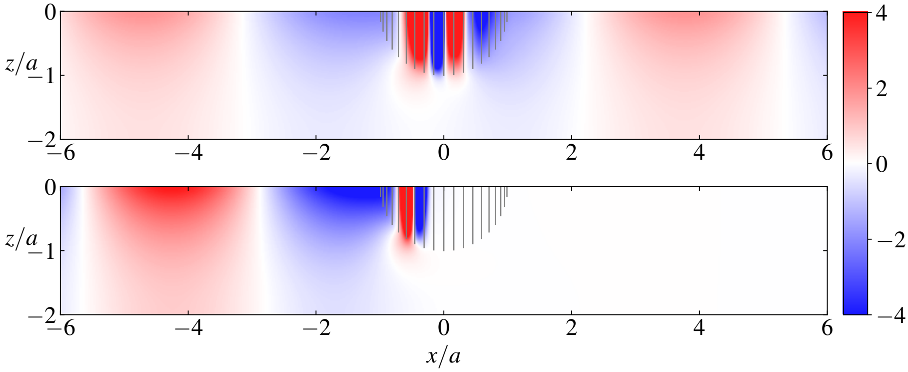

Figure 23: Distribution of the imaginary part of the velocity potential in the flow field for wave scattering by a semi-circular profiled surface-piercing plate-array under normal incidence $\theta_0 = 0°$ at $Ka = 0.958022$ (top panel) and $Ka = 1.092743$ (bottom panel).

wave scattering by horizontal surface-piercing metacylinders. The metacylinders are formed by closely-spaced parallel arrays of thin barriers whose variable length defines the shape of the structure. We have concentrated on square, rectangular, wedge and circular structures in this paper. In each setting, local fluid resonance in the cavities between the plates produces a global effect on the wave field which produces an unorthodox behaviour.

The key novelty of the work is that we have used an exact description of the plate array rather than replacing it by an effective medium. This has allowed us to consider wave frequencies above resonance where the effective medium theory breaks down and where the most interesting results are found. The method of solution that has been used is also novel and has been crucial in simplifying the otherwise complicated interaction between the multiple plate elements of the metastructures. We have shown how to apply transform-based approach in each of the three settings to reduce the problem to a canonical type meaning that all three problems, though superficially quite different, are resolved as solutions to almost identical systems of equations.

A range of results have been produced across the three settings which have been shown to compare favourably to existing results (where that is possible) but showing new results, especially highlighting the role that resonance plays. Arguably, the most interesting results involve graded arrays in which the length of the plates in the array increase with distance into the structure (forming a wedge-shaped metacylinder). This produces a dense spectrum of resonance frequencies associated with the variable length of the cavities in the array and allow for broadbanded "rainbow reflection" effects. We imagine these results will be of interest to coastal engineers developing defence schemes or devices with the potential to manufacture bespoke wave control or harness wave energy. The problems in this paper are set in the context of water waves but the methodology developed herein can be applied to problems in the areas of acoustics, elasticity and electromagnetics.

Appendix A. Far-field scattering waves

The potential in (2.19) indicates that the scattering potential $\phi_{sca} = \phi - \phi_{inc}$ is written as

$$\phi_{sca}(x, y) \approx -\frac{1}{4\pi} \sum_{k=0}^{N} \sum_{p=0}^{2Q+1} a_p^{(k)} \operatorname{sgn}(x - x_k) \int_{-\infty}^{\infty} \int_{-b_k}^{b_k} \mathrm{e}^{-\gamma|x-x_k|+\mathrm{i}\beta(y-y')} w_p(y/b_k)\, \mathrm{d}y'\, \mathrm{d}\beta. \tag{A 1}$$

By using the integral form of the zeroth-order Hankel function (Twersky 1962)

$$H_0(k\varrho) = \frac{1}{\pi \mathrm{i}} \int_{-\infty}^{\infty} \frac{\mathrm{e}^{-\gamma|x-x'|+\mathrm{i}\beta(y-y')}}{\gamma} \mathrm{d}\beta, \qquad \varrho = \sqrt{(x - x')^2 + (y - y')^2} \tag{A 2}$$

where γ has been defined in (2.11) the scattering potential can be rewritten as

$$\begin{aligned} \phi_{sca}(x, y) &\approx -\frac{\mathrm{i}}{4} \sum_{k=0}^{N} \sum_{p=0}^{2Q+1} a_p^{(k)} \int_{-b_k}^{b_k} \left[\frac{\partial}{\partial x'} H_0(k\varrho) \right]_{x'=x_k} w_p(y'/b_k)\, \mathrm{d}y' \\ &= -\frac{\mathrm{i}}{4} \sum_{k=0}^{N} \sum_{p=0}^{2Q+1} a_p^{(k)} \int_{-b_k}^{b_k} \left[\frac{k(x - x')}{\varrho} H_1(k\varrho) \right]_{x'=x_k} w_p(y'/b_k)\, \mathrm{d}y'. \end{aligned} \tag{A 3}$$

In the limit that $kr = k\sqrt{x^2 + y^2} \to \infty$, $\varrho \to r$ and $x - x_k \to \varrho \cos\theta$, $\theta = \tan^{-1}(y/x)$ and using the asymptotic representation of first-order Hankel function for large argument (Abramowitz & Stegun 1964)

$$H_1(kr) \sim \sqrt{\frac{2}{\pi k r}} \mathrm{e}^{\mathrm{i}(kr - 3\pi/4)}, \tag{A 4}$$

the scattering potential in the far field $kr \to \infty$ is approximated as

$$\phi_{sca}(x, y) \sim \sqrt{\frac{2}{\pi k r}} A(\theta; \theta_0) \mathrm{e}^{\mathrm{i}(kr - \pi/4)} \tag{A 5}$$

such that the scattering amplitude $A(\theta; \theta_0)$ is approximated numerically by

$$A(\theta; \theta_0) \approx -\frac{k \cos\theta}{4} \sum_{k=0}^{N} b_k \mathrm{e}^{-\mathrm{i}k x_k \cos\theta} \sum_{p=0}^{2Q+1} a_p^{(k)} D_p(k b_k \sin\theta). \tag{A 6}$$

Acknowledgements. Authors warmly thank Dr. Jin Huang for providing the raw data to verify the algorithm. H. L. was supported by A*STAR Science and Engineering Research Council, Singapore, Grant Number 172 19 00089 under the Marine & Offshore Strategic Research Programme (M&O SRP).

Declaration of interests. The authors report no conflict of interest.

Author ORCID. Authors may include the ORCID identifers as follows. H. Liang, https://orcid.org/0000-0003-3602-1623; R. Porter, https://orcid.org/0000-0003-2669-0188; S. Zheng, https://orcid.org/0000-0001-7124-1619

REFERENCES

Abramowitz, M. & Stegun, I. A. 1964 *Handbook of Mathematical Functions: with Formulas, Graphs, and Mathematical Tables*. National Bureau of Standards.

Bennetts, L.G., Peter, M.A. & Craster, R.V. 2018 Graded resonator arrays for spatial frequency separation and amplification of water waves. *J. Fluid Mech.* **854**, R4.

Bravo, T. & Maury, C. 2023 Broadband sound attenuation and absorption by duct silencers based on the acoustic black hole effect: Simulations and experiments. *J. Sound Vib.* **561**, 117825.

Brûlé, S., Enoch, S. & Guenneau, S. 2020 Emergence of seismic metamaterials: Current state and future perspectives. *Phys. Lett. A.* **384**, 126034.

Chaplain, G.J., Pajer, D., Ponti, J.M. De & Craster, R.V. 2020 Delineating rainbow reflection and trapping with applications for energy harvesting. *New J. Phys.* **22**, 063024.

Colombi, A., Colquitt, D., Roux, P., Guenneau, S. & Craster, R.V. 2016 A seismic metamaterial: The resonant metawedge. *Sci. Rep.* **6** (1), 27717.

Colquitt, D.J., Colombi, A., Craster, R.V., Roux, P., Guenneau, S. & Craster, R.V. 2017 Seismic metasurfaces: sub-wavelength resonators and rayleigh wave interaction. *J. Mech. Phys. Solids* **99**, 379–393.

Gradshtyen, I.S. & Ryhzik, I.M. 1965 *Table of Integrals, Series, and Products*. Academic Press.

Huang, J. & Porter, R. 2023 Water wave propagation through arrays of closely spaced surface-piercing vertical barriers. *J. Fluid Mech.* **960**, A20.

Jan, A.U. & Porter, R. 2018 Transmission and absorption in a waveguide with a metamaterial cavity. *J. Acoust. Soc. Am.* **144** (6), 3172–3180.

Jimenez, N., Romeo-Garcia, V., Pagneux, V. & Groby, J.-P. 2017 Rainbow-trapping absorbers: broadband, perfect and asymmetric sound absorption by subwavelength panels for transmission problems. *Sci. Rep.* **7**, 13595.

Kucher, S., Koźluk, A., Petitjeans, P., Maurel, A. & Pagneux, V. 2023 Backscattering reduction in a sharply bent water wave channel. *Physical Review B* **108** (21), 214311.

Liang, H., Zheng, S., Shao, Y., Cong, P. & Greaves, D. 2023 Wave interactions with a cylinder surrounded by an arc-shaped breakwater. *J. Fluids Struct.* **123**, 104021.

Linton, C.M. & McIver, P. 2001 *Handbook of mathematical techniques for wave/structure interactions*. Chapman Hall/CRC Press, Southampton, UK.

Maier, S. A., ed. 2017 *Handbook Of Metamaterials And Plasmonics (In 4 Volumes)*. World Scientific.

Martin, P. A. 1991 End-point behaviour of solutions to hypersingular integral equations. *Proc. R. Soc. Lond A, Math. Phys. Sci.* **432** (1885), 301–320.

Maruo, H. 1960 The drift force of a body floating in waves. *J. Ship Res.* **4**, 1–10.

Molin, B., Remy, F., Kimmoun, O. & Stassen, Y. 2002 Experimental study of the wave propagation and decay in a channel through a rigid ice-sheet. *Appl. Ocean Res.* **24** (5), 247–260.

Newman, J. N. 1974 Interaction of water waves with two closely spaced vertical obstacles. *J. Fluid Mech.* **66** (1), 97–106.

Noad, I. & Porter, R. 2015 Optimisation of arrays of flap-type oscillating wave surge converters. *Appl. Ocean Res.* **50**, 237–253.

Paris, R.B. 2018 The evaluation of infinite sums of products of Bessel functions. *arXiv preprint arXiv:1803.02757* .

Ponti, J.M. De, Iorio, L. & Ardito, R. 2022 Graded elastic meta-waveguides for rainbow reflection, trapping and mode conversion. *EPJ Appl. Metamat.* **9**, 6.

Porter, R. 2021 Plate arrays as a perfectly-transmitting negative-refraction metamaterial. *Wave Motion* **100**, 102673.

Porter, R. & Evans, D.V. 1995 Complementary approximations to wave scattering by vertical barriers. *J. Fluid Mech.* **294**, 155–180.

Porter, R. & Evans, D.V. 1996 Wave scattering by periodic arrays of breakwaters. *Wave Motion* **23**, 97–120.

Porter, R., Zheng, S. & Liang, H. 2022 Scattering of surface waves by a vertical truncated structured cylinder. *Proceedings of the Royal Society A* **478** (2258), 20210824.

Putley, H.J., Guenneau, S., Craster, R.V., Davies, B. & Poulton, C.G. 2023 Effective properties of periodic plate-array metacylinders. *Physical Review B* **108** (21), 214105.

Putley, H.J., Guenneau, S., Porter, R. & Craster, R.V. 2022 A tunable electromagnetic metagrating. *Proceedings of the Royal Society A* **478** (2268), 20220454.

Roy, R., De, Soumen & Mandal, B.N. 2019 Water wave scattering by multiple thin vertical barriers. *Applied Mathematics and Computation* **355**, 458–481.

Tsakmakidis, K.L., Boardman, A.D. & Hess, O. 2007 Graded resonator arrays for spatial frequency separation and amplification of water waves. *Nature* **450**, 397.

Twersky, V. 1962 On scattering of waves by the infinite grating of circular cylinders. *IRE Transactions on antennas and propagation* **10** (6), 737–765.

Wilks, B., Montiel, F. & Wakes, S. 2022 Rainbow reflection and broadband energy absorption of water waves by graded arrays of vertical barriers. *J. Fluid Mech.* **941**, A26.

Zheng, S., Liang, H. & Greaves, D. 2024 Wave scattering and radiation by a surface-piercing vertical truncated metamaterial cylinder. *J. Fluid. Mech.* **983**, A7.

Zheng, S., Porter, R. & Greaves, D.G. 2020 Wave scattering by an array of metamaterial cylinders. *J. Fluid. Mech.* **903**, A50.

Zhu, J., Chen, Y., Zhu, X., Garcia-Vidal, F.J., Yin, X., Zhang, W. & Zhang, X. 2013 Acoustic rainbow trapping. *Sci. Rep.* **3**, 1728.